19. Moitra J, Mason MM, Olive M *et al.* Life without white fat: a transgenic mouse. *Genes Dev* 1998; **12**: 3168–3181.
20. Ebihara K, Ogawa Y, Masuzaki H *et al.* Transgenic overexpression of leptin rescues insulin resistance and diabetes in a mouse model of lipoatrophic diabetes. *Diabetes* 2001; **50**: 1440–1448.
21. Kjeldsen L, Johnsen AH, Sengeløv H *et al.* Isolation and primary structure of NGAL, a novel protein associated with human neutrophil gelatinase. *J Biol Chem* 1993; **268**: 10425–10432.
22. Brenner BM, Cooper ME, de Zeeuw D *et al.* RENAAL Study Investigators. Effects of losartan on renal and cardiovascular outcomes in patients with type 2 diabetes and nephropathy. *N Engl J Med* 2001; **345**: 861–869.
23. Bolignano D, Coppolino G, Campo S *et al.* Urinary neutrophil gelatinase-associated lipocalin (NGAL) is associated with severity of renal disease in proteinuric patients. *Nephrol Dial Transplant* 2008; **23**: 414–416.
24. Tucker BJ, Rasch R, Blantz RC. Glomerular filtration and tubular reabsorption of albumin in preproteinuric and proteinuric diabetic rats. *J Clin Invest* 1993; **92**: 686–694.
25. Tojo A, Onozato ML, Kurihara H *et al.* Angiotensin II blockade restores albumin reabsorption in the proximal tubules of diabetic rats. *Hypertens Res* 2003; **26**: 413–419.
26. Birn H, Christensen EI. Renal albumin absorption in physiology and pathology. *Kidney Int* 2006; **69**: 440–449.
27. Osicka TM, Houlihan CA, Chan JG *et al.* Albuminuria in patients with type 1 diabetes is directly linked to changes in the lysosome-mediated degradation of albumin during renal passage. *Diabetes* 2000; **49**: 1579–1584.
28. Chouinard S, Viau C. Reversibility of renal tubular dysfunction in streptozotocin-induced diabetes in the rat. *Can J Physiol Pharmacol* 1992; **70**: 977–982.
29. Brezniceanu ML, Liu F, Wei CC *et al.* Attenuation of interstitial fibrosis and tubular apoptosis in db/db transgenic mice overexpressing catalase in renal proximal tubular cells. *Diabetes* 2008; **57**: 451–459.
30. Manotham K, Tanaka T, Matsumoto M *et al.* Evidence of tubular hypoxia in the early phase in the remnant kidney model. *J Am Soc Nephrol* 2004; **15**: 1277–1288.
31. Onozato ML, Tojo A, Goto A *et al.* Oxidative stress and nitric oxide synthase in rat diabetic nephropathy: effects of ACEI and ARB. *Kidney Int* 2002; **61**: 186–194.
32. Zatz R, Dunn BR, Meyer TW *et al.* Prevention of diabetic glomerulopathy by pharmacological amelioration of glomerular capillary hypertension. *J Clin Invest* 1986; **77**: 1925–1930.
33. Breyer MD, Böttinger E, Brosius III FC *et al.* Mouse models of diabetic nephropathy. *J Am Soc Nephrol* 2005; **16**: 27–45.
34. Ichinose K, Maeshima Y, Yamamoto Y *et al.* Antiangiogenic endostatin peptide ameliorates renal alterations in the early stage of a type 1 diabetic nephropathy model. *Diabetes* 2005; **54**: 2891–2903.
35. Yan QW, Yang Q, Mody N *et al.* The adipokine lipocalin 2 is regulated by obesity and promotes insulin resistance. *Diabetes* 2007; **56**: 2533–2540.
36. Hvidberg V, Jacobsen C, Strong RK *et al.* The endocytic receptor megalin binds the iron transporting neutrophil-gelatinase-associated lipocalin with high affinity and mediates its cellular uptake. *FEBS Lett* 2005; **579**: 773–777.
37. Keppler A, Gretz N, Schmidt R *et al.* Plasma creatinine determination in mice and rats: an enzymatic method compares favorably with a high-performance liquid chromatography assay. *Kidney Int* 2007; **71**: 74–78.
38. Kosugi R, Shioi T, Watanabe-Maeda K *et al.* Angiotensin II receptor antagonist attenuates expression of aging markers in diabetic mouse heart. *Circ J* 2006; **70**: 482–488.
39. Shao J, Iwashita N, Ikeda F *et al.* Beneficial effects of candesartan, an angiotensin II type 1 receptor blocker, on beta-cell function and morphology in db/db mice. *Biochem Biophys Res Commun* 2006; **344**: 1224–1233.
40. Nagae T, Mori K, Mukoyama M *et al.* Adrenomedullin inhibits connective tissue growth factor expression, extracellular signal-regulated kinase activation and renal fibrosis. *Kidney Int* 2008; **74**: 70–80.
41. Yokoi H, Mukoyama M, Mori K *et al.* Overexpression of connective tissue growth factor in podocytes deteriorates diabetic nephropathy in mice. *Kidney Int* 2008; **73**: 446–455.

Cardiovascular Research (2009) 83, 682–687
doi:10.1093/cvr/cvp171

The cardiac pacemaker-specific channel *Hcn4* is a direct transcriptional target of MEF2

Shinobu Kuratomi[1], Yoko Ohmori[1], Masayuki Ito[1], Kuniko Shimazaki[1], Shin-ichi Muramatsu[2], Hiroaki Mizukami[3], Hideki Uosaki[4], Jun K. Yamashita[4], Yuji Arai[5], Koichiro Kuwahara[6], and Makoto Takano[1]*

[1]*Department of Physiology, School of Medicine, Jichi Medical University, Shimotsuke, Tochigi 329-0498, Japan;* [2]*Division of Neurology, Department of Medicine, School of Medicine, Jichi Medical University, Shimotsuke, Tochigi 329-0498, Japan;* [3]*Division of Genetic Therapeutics, Center for Molecular Medicine, Jichi Medical University, Shimotsuke, Tochigi 329-0498, Japan;* [4]*Laboratory of Stem Cell Differentiation, Stem Cell Research Center, Institute for Frontier Medical Sciences, Kyoto University, Kyoto 606-8507, Japan;* [5]*Department of Bioscience, National Cardiovascular Center Research Institute, Suita, Osaka 565-8565, Japan; and* [6]*Department of Medicine and Clinical Sciences, Graduate School of Medicine, Kyoto University, Kyoto 606-8507, Japan*

Received 21 January 2009; revised 8 May 2009; accepted 22 May 2009; online publish-ahead-of-print 28 May 2009

Time for primary review: 34 days

KEYWORDS
Hcn4;
MEF2;
Sino-atrial node;
Channel;
Transcription

Aims *Hcn4*, which encodes the hyperpolarization-activated, cyclic nucleotide-sensitive channel (I_h), is a well-established marker of the cardiac sino-atrial node. We aimed to identify *cis*-elements in the genomic locus of the *Hcn4* gene that regulate the transcription of *Hcn4*.

Methods and results We screened evolutionarily conserved non-coding sequences (CNSs) that are often involved in the regulation of gene expression. The VISTA Enhancer Browser identified 16 regions, termed CNS 1-16, within the *Hcn4* locus. Using the luciferase reporter assay in primary neonatal rat cardiomyocytes, we found that CNS13 conferred a prominent enhancer activity (more than 30-fold) on the *Hcn4* promoter. Subsequent mutation analysis revealed that the *Hcn4* enhancer function was dependent on myocyte enhancer factor-2 (MEF2) and activator protein-1 (AP1) binding sequences located in CNS13. Electrophoretic mobility shift assay and chromatin immunoprecipitation confirmed that MEF2 and AP1 proteins bound CNS13. Furthermore, overexpression of a dominant negative MEF2 mutant inhibited the enhancer activity of CNS13, decreased *Hcn4* mRNA expression and also decreased the amplitude of I_h current in myocytes isolated from the inflow tract of embryonic heart.

Conclusion These results suggest that the novel enhancer CNS13 and MEF2 may play a critical role in the transcription of *Hcn4* in the heart.

1. Introduction

The appropriate timing of cardiac muscle contraction is regulated by the electrical conduction system of the heart and consists of cardiomyocytes possessing specialized electrical function. The precise expression pattern of cardiac ion channel genes in relation to such electrophysiological properties has been extensively studied.[1,2] Previous reports have demonstrated that the hyperpolarization-activated, cyclic nucleotide-sensitive cation current (I_h) encoded by the *Hcn4* gene appears one of the ion currents underlying pacemaker depolarization.[3,4] In mammalian adult heart, *Hcn4* is specifically expressed in the sino-atrial node (SAN). During development *Hcn4* is also expressed in the foetal and neonatal chamber myocardium. As a result of this distribution, *Hcn4* is now recognized as a key marker gene of the SAN.[5,6] Despite its role as an SAN marker, little is known about the *cis*-elements that directly regulate *Hcn4* expression. Progress in the genome project and comparative genomic-base approaches have proven useful in the identification of gene regulatory sequences in a wide range of genomic loci.[7,8] We have previously reported that an 847 bp proximal sequence induces minimal promoter activity of the *Hcn4* gene.[9] In addition to this proximal upstream region, we also identified conserved, non-coding sequences within the *Hcn4* gene locus and analysed their enhancer function. We found that the novel enhancer contained binding sites for activator protein-1 (AP1) and myocyte enhancer factor-2 (MEF2) and played a critical role in the expression of *Hcn4*. These results outline the potential mechanisms underlying SAN differentiation.

* Corresponding author. Tel: +81 285 58 7308; Fax: +81 285 40 6294.
E-mail address: takanom@jichi.ac.jp

2. Methods

2.1 Construction of the promoter reporter plasmid

Luciferase reporter constructs were prepared using pGL4.10 vector (Promega) and the *Hcn4* promoter construct was obtained as previously described.[9] Conserved non-coding sequence (CNS) fragments were isolated from mouse genomic DNA by PCR with the primer pairs listed in Supplementary material online, *Table S1* and were subcloned into the upstream region of the *Hcn4* promoter.

2.2 Cell culture

For the culture of neonatal cardiomyocytes, 1- to 2-day-old rats were decapitated, the ventricle rapidly dissected and myocytes isolated by collagenase digestion (Worthington, type 2, 80 U/mL). The myocytes were then enriched by discontinuous Percoll gradient centrifugation (yield more than 90%).

For the culture of embryonic cardiomyocytes, rat embryos (13 days after fertilization) were removed from pregnant rats under deep anaesthesia with ether, the inflow tract of embryonic heart dissected and the primordial right and left appendixes removed. Myocytes were then isolated using the same procedure as that for the culture of neonatal myocytes.

Embryonic and neonatal cardiomyocytes were plated at a density of 2×10^4 and 10^5 cells/well, respectively, in 24-well plates and cultured in DMEM with 10% foetal bovine serum.[9]

All experiments were approved in advance by the animal Ethics Committee of Jichi Medical University. The investigation conforms with the Guide for the Care and Use of Laboratory Animals published by the US National Institutes of Health (NIH Publication No. 85-23, revised 1996).

2.3 Luciferase reporter gene assay

Luciferase reporter constructs (0.5 μg) and pGL4.74 vector (0.03 μg) were co-transfected into neonatal cardiomyocytes using Lipofectamine LTX (Invitrogen). Luciferase activities were measured 3 days after the transfection using the Dual-Luciferase Reporter Assay System (Promega). Transcriptional activities were obtained from three separate assays performed in quadruplicate.

2.4 Electrophoretic mobility shift assays

The myc-tagged mouse c-Jun/AP1 and MEF2C proteins were *in vitro* translated using TNT Quick Coupled Transcription/Translation System (Promega) and CNS13 DNA probes radiolabelled with [^{32}P]. The binding reaction was then performed in a reaction buffer (final volume=20 μL) containing 20 mM HEPES (pH 7.6), 50 mM KCl, 1 mM $MgCl_2$, 0.1% Nonidet P-40, 5% glycerol, 5 mM dithiothreitol, 1 mM EDTA, and 1 μg poly(dI-dC). The probe (10 fmol) incubated with 1 μL of protein was analysed on 4% polyacrylamide gels in ×0.25 TBE buffer. In competition experiments, 100-fold molar excess of double-strand oligonucleotides (AP1: 5′-ATT CTG AGT CAG AGA-3′ and MEF2: 5′-AGG TGG GTT AAA AAT AGA GCC CT-3′) were added.

2.5 Chromatin immunoprecipitation

Chromatin isolated from neonatal rat cardiomyocytes was immunoprecipitated with specific antibodies directed against anti-c-Jun/AP1 (Calbiochem) and anti-MEF2 (AnaSpec) using the EZ chromatin immunoprecipitation (ChIP) assay kit (Upstate) and analysed by PCR using the following primer pairs: CNS13 ChIP primers 5′-CCT TGG TTG TGA GTC TGT GTC T-3′ (forward) and 5′-AGT GGA GAG ACT GCT CTT TTC C-3′ (reverse) and control ChIP primers 5′-AAT GGG ACT CCT CTT ACT CAT TTC T-3′ (forward) and 5′-AAA GTC CCT GAT GAC ACA CTA GTT C-3′ (reverse).

2.6 AAV vector production and transfection

Adeno-associated virus (AAV) vector plasmids contain an expression cassette consisting of a CMV promoter followed by the first intron of human growth hormone, target cDNA, woodchuck hepatitis virus post-transcriptional regulatory element (GenBank accession no. J04514) and the SV40 poly-A signal sequence, between the inverted terminal repeats of the AAV-3 genome. The plasmids pAAV-dnMEF2 and pAAV-GFP contained the cDNA of the dominant negative MEF2 (dnMEF2) fused with Orange fluorescent protein (Clontech) and GFP, respectively. The two helper plasmids, pHelper (Agilent) and pAAV1-RC, harbour the *E2A*, *E4*, and *VA RNA* genes of the adenovirus genome, and the AAV-1 *rep* and *cap* genes, respectively. HEK293 cells were cotransfected using the calcium phosphate coprecipitation method with the vector plasmid, pAAV1-RC and pHelper. AAV1 vectors were harvested and purified via two sequential continuous iodoxale ultracentrifugations. The vector titer was determined by quantitative PCR (Q-PCR) of DNase I-treated vector stocks, yielding 10^{11}–10^{12} vector genome copies (vg).[12] 2×10^4 foetal myocytes were transfected with 10^{10} vg AAV1-dnMEF2 or AAV1-EGFP; and 10^5 vg Empty AV5 vector was also transfected as a helper.

2.7 RT-PCR and Q-PCR analysis

Three days after the transfection of AAV1, total RNA was isolated from primary cultured embryonic myocytes using TRIZOL reagent (Invitrogen). Single-strand cDNA was synthesized using Superscript III (Invitrogen). Q-PCR was carried out with predesigned Taqman Probes for *hcn4*, *hcn2*, *hcn1*, *stars*, and the 18s rRNA, in an ABI Prism 7700 System (Applied Biosystems).

2.8 Immunostaining of cardiomyocytes

Cardiomyocytes were fixed with 4% paraformaldehyde and incubated with primary antibodies directed against HCN4 (1:200 dilution; Chemicon) and actinin (1:750; Monoclonal, Sigma). Following extensive washes, cells were incubated with Alexa Fluor 488-conjugated anti-rabbit or anti-mouse Ig secondary antibodies at a concentration of 1:500 (Molecular Probes).

2.9 Electrophysiological analysis

Electrophysiological measurements were carried out using an Axopatch200B amplifier and a Digidata 1320 interface (Axon). The bathing solution contained 140 mM NaCl, 5.4 mM KCl, 0.33 mM NaH_2PO_4, 0.5 mM $MgCl_2$, 1.8 mM $CaCl_2$, 0.5 mM $BaCl_2$, 5 mM HEPES (pH 7.4 with NaOH), and the standard high K^+ pipette solution contained 110 Aspartic acid, 30 mM KCl, 5 mM MgATP, 5 mM Na_2 creatine phosphate, 0.1 mM Na_2GTP, 2 mM EGTA, 10 mM HEPES (pH 7.2 with KOH).

2.10 Statistical analysis

Data are expressed as mean ± SD values. Statistical analysis was performed using the Student's *t*-test and $P < 0.05$ was defined as statistically significant.

3. Results

3.1 Functional analysis of conserved non-coding regions within the *Hcn4* gene locus

Our previous study revealed that the proximal 847 bp sequence in the *Hcn4* upstream region is essential for promoter activity.[9] In order to locate additional *cis*-regulatory sequences, we extensively searched the CNSs in the genomic locus of *Hcn4*. As illustrated in *Figure 1A*, we identified 16 regions using VISTA Enhancer Browser, and designated these regions CNS 1-16 (Supplementary material online, *Table S1*).[8]

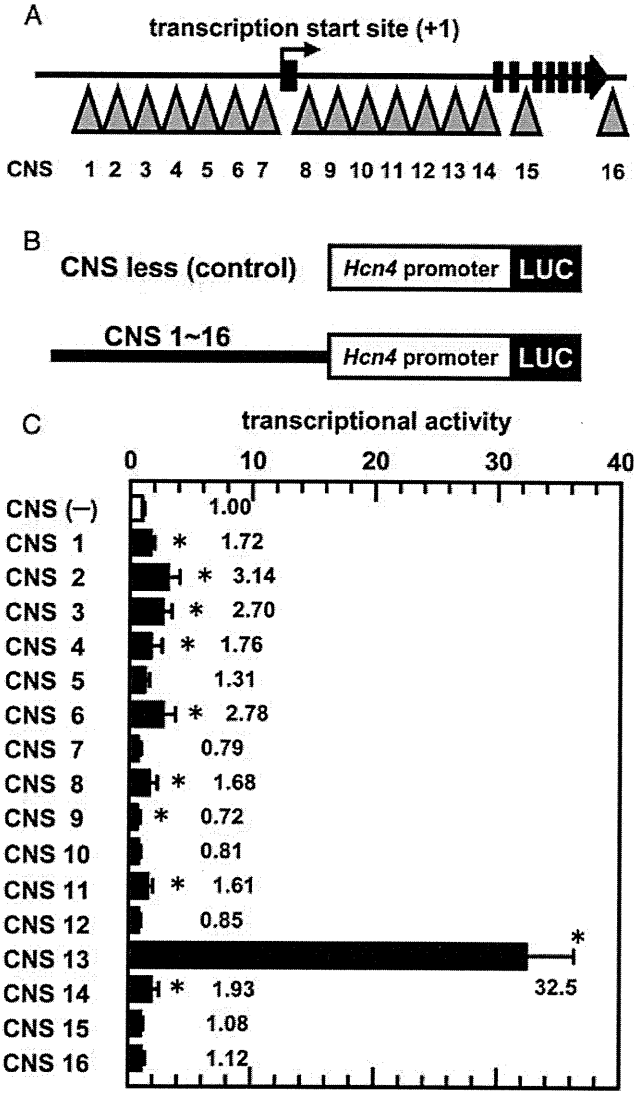

Figure 1 Enhancer activity of the CNS fragments. (*A*) A schematic diagram outlining the genomic organization of the murine *Hcn4* gene. Arrows indicate CNS regions. (*B*) Structure of the luciferase reporter constructs. The *Hcn4* promoter comprises nucleotides −446 to +400 relative to the transcription start site. (*C*) Enhancer activity conferred by the CNS fragments. Data are presented as relative values to the activity of the *Hcn4* promoter. $^*P < 0.05$ compared with construct of *Hcn4* promoter alone.

We next evaluated enhancer activity for each of the CNS regions using the luciferase reporter assay. In order to achieve this, we linked CNS fragments to the *Hcn4* promoter expressing the luciferase reporter gene in the pGL4.10 vector (*Figure 1B*) and analysed enhancer function in cultured primary cardiomyocytes. As shown in *Figure 1C*, nine CNS fragments (CNS1, 2, 3, 4, 6, 8, 11, 13, and 14) significantly enhanced *Hcn4* promoter activity. The CNS13 construct led to an ~33-fold increase in transcriptional activity, in comparison to the remainder of the constructs that resulted in no more than a 3.2-fold increase.

3.2 MEF2 and AP1 sites are required for the enhancer activity of CNS13

To confirm that CNS13 acts as an authentic enhancer, we next constructed inverted CNS13 and tandem repeated CNS13 fragments and fused with the *Hcn4* promoter. As

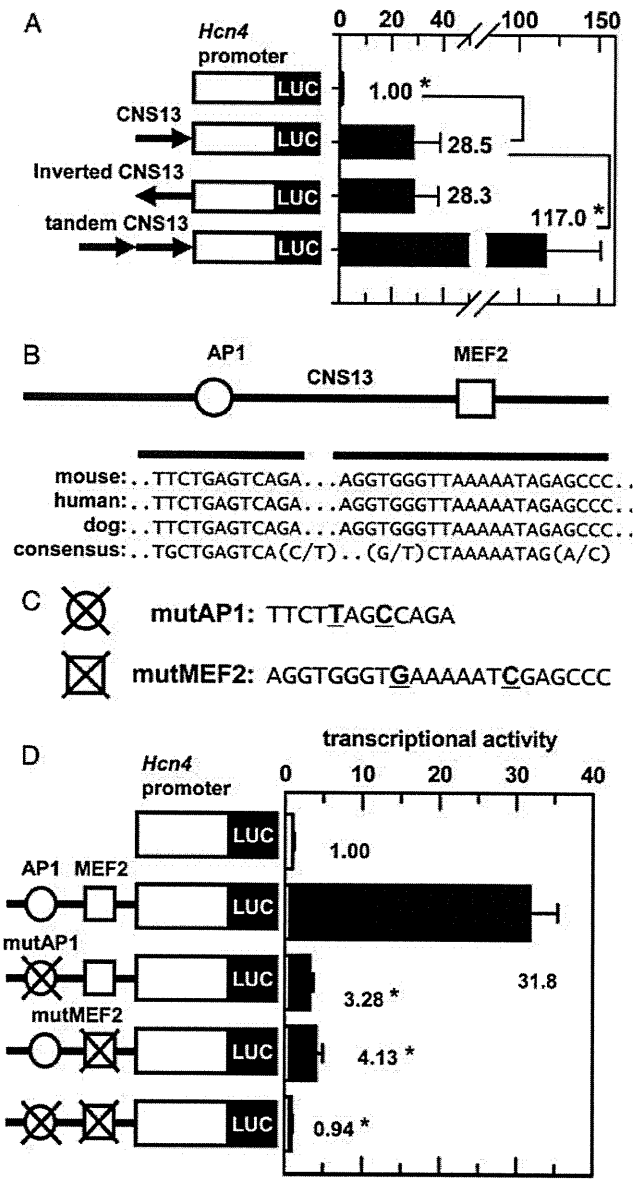

Figure 2 MEF2 and AP1 sites are essential in CNS13. (*A*) A schematic diagram of control, inverted, and tandem CNS13 constructs. The inverted construct was made by swapping the restriction sites at the ends of the control CNS13 fragment. The tandem construct, by introducing *Eco*RI site between the fragments. $^*P < 0.05$ compared with control CNS13 construct. (*B*) A schematic diagram of the putative binding sequences for AP1 (open circle) and MEF2 (open square) in CNS13. The AP1 and MEF2 sequences in mouse, human, and dog are aligned with the consensus sequences. The score for the matches were AP1: core match 1.000; matrix match 0.923. MEF2: core match 1.000; matrix match 0.957. (*C*) Mutation of the AP1 and MEF2 sites. The bold, underlined characters indicate the substituted nucleotides. (*D*) Enhancer activity of the CNS13 mutants. Data is presented as relative values to the activity of the *Hcn4* promoter. $^*P < 0.05$ compared with *Hcn4* promoter.

shown in *Figure 2A*, no significant difference was found between the enhancer activities of normal- and inverted-CNS13 fragments. Tandem repeat CNS13 robustly activated the *Hcn4* promoter. We then focused our study on the CNS13 sequence and explored its *cis*-regulatory mechanism and its potential as a novel enhancer for the *Hcn4* promoter.

To characterize functional motifs in the CNS13 sequence, we searched putative transcription factor binding sites using

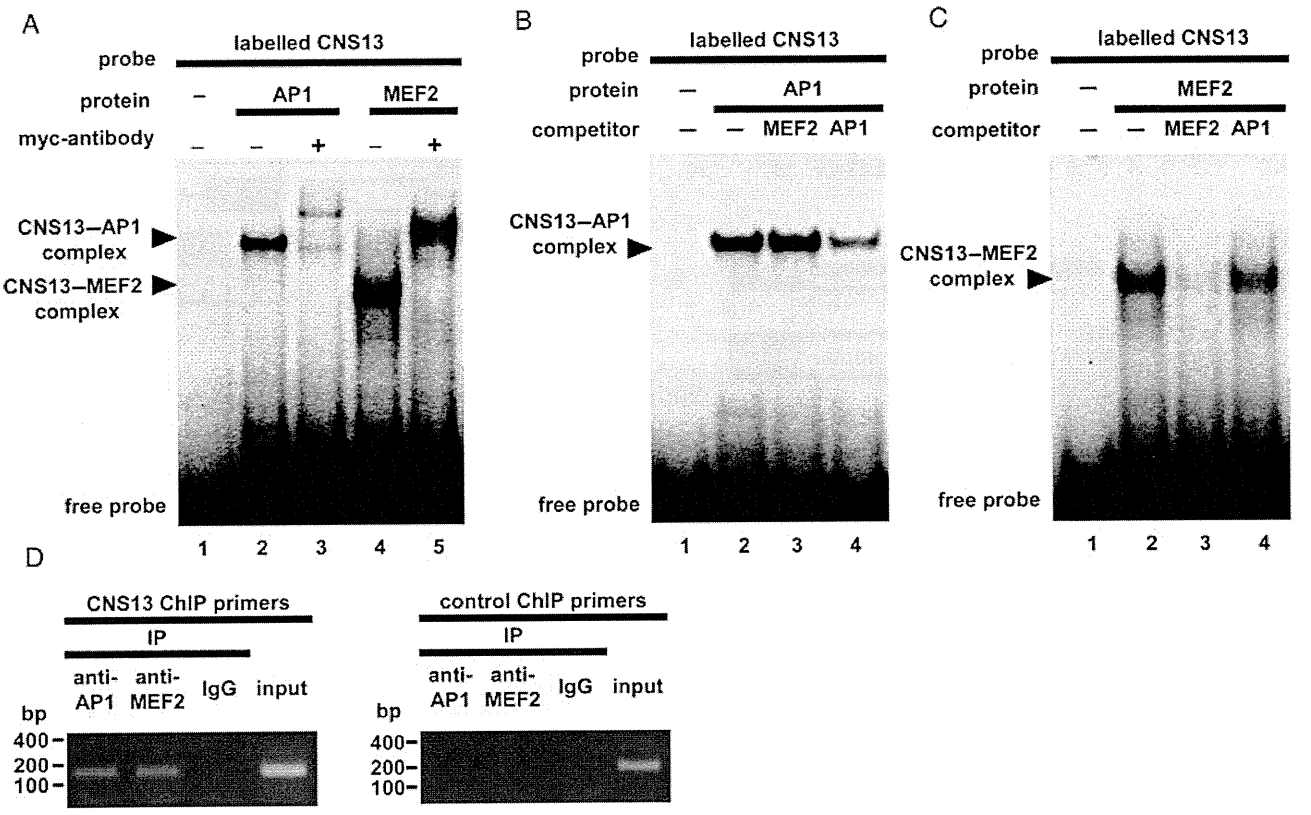

Figure 3 Electrophoretic mobility shift assay (EMSA) and chromatin immunoprecipitation (ChIP) assay using a radiolabelled CNS13 probe. (*A*) EMSA with myc-tagged AP1 and MEF2 proteins. The myc-antibody was used for the supershift assay. (*B*) Competitive EMSAs for the CNS13–AP1 complex. (*C*) CNS13–MEF2 complexes. (*D*) ChIP products using specific antibodies directed against AP1 and MEF2, or a pre-immune IgG were analysed by PCR. Input lane represents PCR products amplified from sonicated chromatin prior to immunoprecipitation. The 152 bp (left) and 200 bp (right) products correspond to CNS13 and distinct genomic regions, respectively.

the TRANSFAC database and detected MEF2- and AP1-binding motifs. As shown in *Figure 2B*, the putative MEF2- and AP1-binding sequences are perfectly conserved among several mammalian species and closely resemble their consensus sequences. These motifs, however, were not conserved in non-mammalian species. We prepared CNS13 reporter constructs harbouring mutations within the MEF2 and AP1 sites (*Figure 2C*) and examined whether enhancer activity was mediated by these sites. As shown in *Figure 2D*, a single mutation in either MEF2- or AP1-binding sequences significantly reduced transcriptional activity, whereas double mutations completely abolished CNS13-induced enhancement. These findings indicate that the *cis*-enhancer function of the CNS13 fragment is dependent on these binding sequences.

We then examined binding of MEF2 and AP1 protein to CNS13. As demonstrated by the electrophoretic mobility shift assay (EMSA) outlined in *Figure 3A*, a slow-migrating band was visualized as a result of interaction between the CNS13 probe and the myc-tagged AP1 protein (lane 2). Another complex was also formed when myc-tagged MEF2 protein was co-incubated with the CNS13 probe (lane 4). Myc-antibody also formed additional complexes (lanes 3 and 5). To precisely identify the DNA sequences recognized by MEF2 and AP1 proteins, we performed competitive EMSA using unlabelled competitors composed of partial CNS13 sequences. As shown in *Figrue 3B*, the signal for the CNS13–AP1 complex was attenuated by the addition of AP1 competitor (lane 4), but not MEF2 competitor (lane 3), indicating that the complex formation is AP1-sequence specific. In CNS13–MEF2 complex competition assays, the opposite patterns were observed (*Figure 3C*). In addition, we amplified a genomic DNA fragment of CNS13 using ChIP with antibodies directed against AP1 and MEF2 (*Figure 3D*). These findings strongly suggest that MEF2 and AP1 transcription factors bind to CNS13 and play an important physiological role in *Hcn4* transcription.

3.3 dnMEF2 resulted in reduced Hcn4 expression

Among the MEF2 family of transcription factors, *MEF2A*, *C*, and *D* are expressed in cardiomyocytes.[10] Given that AP1 is a ubiquitously expressed transcription factor, we focused our study on the physiological role of MEF2. It has previously been shown that MEF2 proteins form hetero- and homodimers and that overexpression of dnMEF2 inhibit its transcriptional activity.[11] The schematic in *Figure 4A* outlines the structure of dnMEF2. In the current study, we demonstrate that dnMEF2 significantly reduced the transcriptional activity of the luciferase reporter vectors and that the enhancer activity of CNS13 was attenuated to 12% of the control levels. When MEF2 binding motif of CNS13 was disrupted, the overexpression of dnMEF2 did not significantly inhibit the enhancer activity (*Figure 4B*).

In order to examine the physiological role of *MEF2 in vivo*, we next expressed dnMEF2 using the AAV1 vector in cardiomyocytes isolated from the inflow tract of the embryonic rat heart, a site in which the HCN4 channel is highly

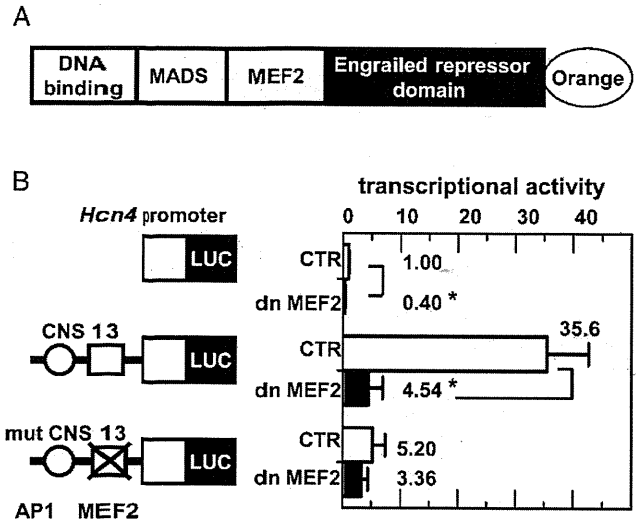

Figure 4 dnMEF2 inhibits *Hcn4* enhancer activity. (*A*) A schematic of the structure of dominant negative MEF2 mutant originated from MEF2C. (*B*) Transcriptional activity of the *Hcn4* promoter and CNS13, but not MEF2 site mutated CNS13, are significantly suppressed by dnMEF2. Along with luciferase reporter constructs, pAAV-dnMEF2 (0.3 μg) or pAAV-GFP (control; 0.3 μg) plasmids were cotransfected. Data are presented as relative values to the activity of the *Hcn4* promoter ($n = 4$; $^*P < 0.05$).

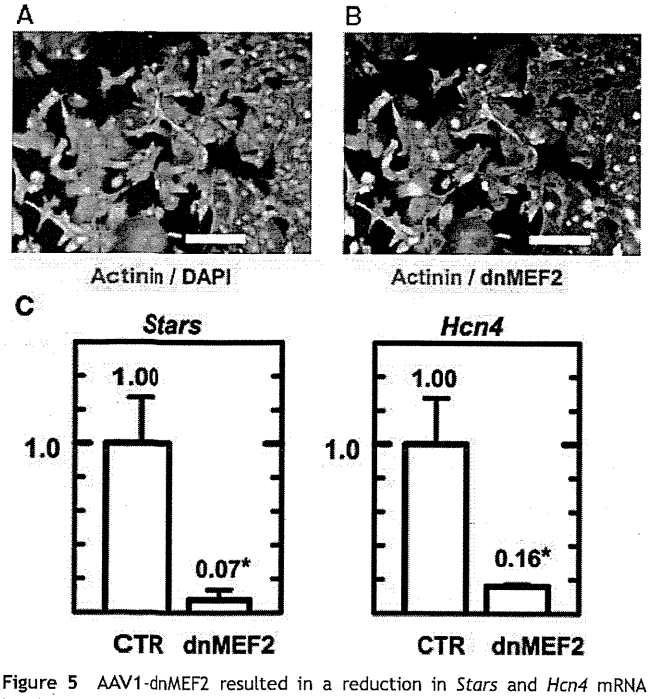

Figure 5 AAV1-dnMEF2 resulted in a reduction in *Stars* and *Hcn4* mRNA levels. (*A*) Immunofluorescent staining of cardiomyocytes for actinin (green). Nucleus is counter stained with DAPI (blue). Approximately 99% of the cells are actinin positive. Bar, 100 μm. (*B*) AAV1-dnMEF2 transfected myocytes demonstrate a nuclear orange fluorescent signal. Approximately 70% of the cells are transfected. (*C*) Relative mRNA levels measured by Q-PCR. Left, *Stars*. Right, *Hcn4*. ($n = 4$; $^*P < 0.05$ vs. control).

expressed.[12] As shown in *Figure 5A*, ~70% of cardiomyocytes was successfully transfected with dnMEF2. Three days following the transfection, *Hcn4* expression levels of Hcn4 were evaluated using real-time PCR. We also evaluated the expression levels of striated muscle activator of Rho signalling (*Stars*), which is known as a direct transcriptional target of MEF2.[13] As shown in *Figure 5A* and *B*, we found

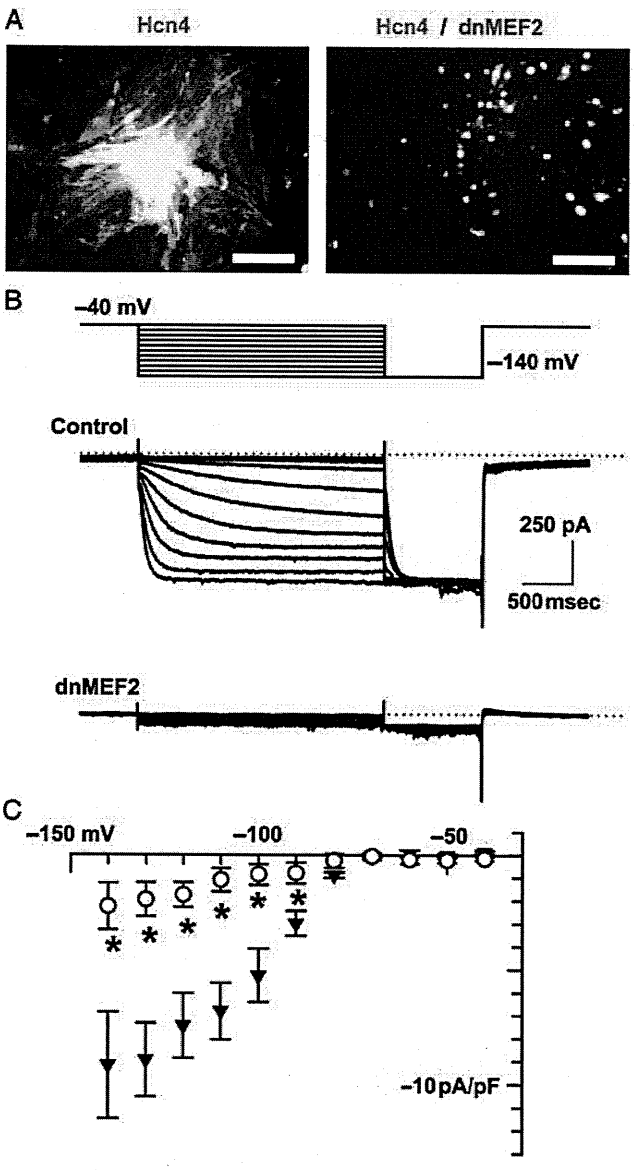

Figure 6 AAV1-dnMEF2 suppressed functional expression of the HCN4 channel. (*A*) Immunostaining for HCN4 (green). Left, control. Right, AAV1-dnMEF2. Bar, 100 μm. (*B*) I_h recorded in embryonic myocytes. The pulse protocol is shown in the top panel. The dotted line indicates the zero current level. (*C*) Current–voltage diagram of I_h. The amplitude of time-dependent current elicited by hyperpolarization was normalized by cellular capacitance. Filled triangle, control; open circle, dnMEF2 ($n = 7$; $^*P < 0.05$).

that both *Stars* and *Hcn4* mRNA levels were significantly reduced in dnMEF2-transfected myocytes, when compared with GFP-transfected myocytes as the negative control. In dnMEF2-transfected myocytes, however, the mRNA levels of HCN1 and HCN2, other types of HCN channels expressed in the heart, were not changed significantly (Supplementary material online, *Figure S1*). These channels might be regulated by different transcriptional mechanisms.[14]

We finally examined the functional expression of the HCN4 channel in embryonic myocytes transfected with dnMEF2. As shown in *Figure 6A* (left panel), HCN4 protein was clearly identified in control myocytes. However, only faint staining of HCN4 protein was observed in the myocytes transfected with dnMEF2 (nuclear-localized orange signals). In accordance with this, robust I_h current was also recorded in the control myocytes (*Figure 6B*, upper traces), whereas I_h

current was significantly reduced in dnMEF2-transfected myocytes (*Figure 6B*, lower traces). *Figure 6C* outlines the current–voltage diagram. The amplitude of I_h in dnMEF2-transfected myocytes was ~18% of the control myocytes. Similar results were also obtained for ES-derived cardiomyocytes (data not shown).[15]

4. Discussion

The transcription factors AP1 and MEF2 are known to play a variety of roles in the development of the heart. It has been reported that the ablation of *c-jun*, who along with *c-fos* forms the AP1 transcription factor, gave rise to the anomalies of right ventricular outflow tract and a reduction in *Cx43* expression.[16] Although we did not examine the direct physiological role of AP1 in the present study, it appears reasonable to expect that the expression of the *Hcn4* gene might also be reduced following the deletion of the AP1 protein. During development, *MEF2C* is known to be the predominant form of *MEF2* expressed in the embryonic heart. *MEF2A* and *MEF2D* became the major *MEF2* forms after birth.[10] Gene knockout of *MEF2C* results in an embryonic lethal phenotype.[17] MEF2D$^{-/-}$ mice are viable, demonstrating a weak response to hypertrophic stimulation.[18] *MEF2A* knockout mice generated on a 129Sv background die immediately following birth and demonstrate sinus arrhythmia and conduction block.[19] As the present study demonstrates that the expression of *Hcn4* is dependent on MEF2, it would be interesting to explore the ion channel expression in SAN of *MEF2A*$^{-/-}$ animals.

Recent studies have suggested that the *Nkx2-5* and *Pitx2c* transcription factors repress the expression of *Hcn4* in chamber myocardium, a result that is likely due to the inhibition of activators.[16] However, activators of *Hcn4* have not been identified in cardiomyocytes to date. The results of the current study suggest that MEF2 and AP1 may be candidate activators. The transcription factor *Tbx3*, in addition to *Hcn4*, is also specifically expressed in SAN. Ectopic expression of *Tbx3* in the atrium is known to induce *Hcn4* expression. However, it remains unclear whether *Hcn4* is a direct target of *Tbx3*.[5] Interestingly, we identified conserved MEF2- and AP1-like sequences within the *tbx3* gene locus. The spatiotemporal expression of *Tbx3* and *Hcn4* might be regulated via similar mechanisms.

MEF2 expression in the heart has been shown to be increased in the atrium.[20] Therefore, regional differences in *MEF2* expression might account in part for the spatial distribution of *Hcn4*. In this respect, it appears to be particularly important to investigate whether CNS13 is able to reproduce the spatiotemporal expression pattern of *Hcn4* in the heart. Although we have generated transgenic mice harbouring a *LacZ* reporter gene driven by the CNS13 and *Hcn4* promoter, we were unable to obtain consistent patterns of β-gal expression in embryos (data not shown). Thus, it is speculated that a combination of multiple CNSs may be required to reproduce the precise spatiotemporal expression pattern of *Hcn4*. Future studies will be required to address this question.

Supplementary material

Supplementary Material is available at *Cardiovascular Research* online.

Acknowledgements

We thank Dr M.A. Arnold for providing the dominant negative MEF2 cDNA.

Conflict of interest: none declared.

Funding

This work was supported in part by a Grant from the Vehicle Racing Commemorative Foundation and a Grant-in-Aid for Scientific Research from JSPS (#20300141).

References

1. Shram G, Pourrier M, Melnyk P, Nattel S. Differential distribution of cardiac ion channel expression as a basis for regional specialization in electrical function. *Circ Res* 2002;**90**:939–950.
2. Marionneau C, Couette B, Liu J, Mangoni M-E, Nargeot J, Lei M *et al.* Specific pattern of ion channel gene expression associated with pacemaker activity in the mouse heart. *J Physiol* 2005;**562**:223–234.
3. Ishii TM, Takano M, Xie L-H, Noma A, Ohmori H. Molecular characterization of the hyperpolarization-activated cation channel in rabbit heart sinoatrial node. *J Biol Chem* 1999;**274**:12835–12839.
4. Hermann S, Stieber J, Ludwig A. Pathophysiology of HCN channels. *Pflügers Arch* 2007;**454**:517–522.
5. Hoogaars W-M, Engel A, Brons J-F, Verkerk A-O, de Lange F-J, Wong L-Y *et al.* Tbx3 controls the sinoatrial node gene program and imposes pacemaker function on the atria. *Genes Dev* 2007;**21**:1098–1112.
6. Mommersteeg M-T, Hoogaars W-M, Prall O-W, de Gier-de Vries C, Wiese C, Clout D-E *et al.* Molecular pathway for the localized formation of the sinoatrial node. *Circ Res* 2007;**100**:354–362.
7. Pennacchio L-A, Ahituv N, Moses A-M, Prabhakar S, Nobrega M-A, Shoukry M *et al. In vivo* enhancer analysis of human conserved non-coding sequences. *Nature* 2006;**444**:499–502.
8. Visel A, Minovitsky S, Dubchak I, Pennacchio L-A. VISTA Enhancer Browser—a database of tissue-specific human enhancers. *Nucleic Acids Res* 2007;**35**:D88–D92.
9. Kuratomi S, Kuratomi A, Kuwahara K, Ishii TM, Nakao K, Saito Y *et al.* NRSF regulates the developmental and hypertrophic changes of HCN4 transcription in rat cardiac myocytes. *Biochem Biophys Res Commun* 2007;**353**:67–73.
10. Potthoff M-J, Olson E-N. MEF2: a central regulator of diverse developmental programs. *Development* 2007;**134**:4131–4140.
11. Arnold M-A, Kim Y, Czubryt M-P, Phan D, McAnlly J, Qi X *et al.* MEF2C transcription factor controls chondrocyte hypertrophy and bone development. *Dev Cell* 2007;**12**:377–389.
12. Li X-G, Okada T, Kodera M, Nara Y, Takino N, Muramatsu C *et al.* Viral-mediated temporally controlled dopamine production in a rat model of Parkinson disease. *Mol Ther* 2006;**13**:160–166.
13. Kuwahara K, Teg Pipes G-C, McAnally J, Richardson J-A, Hill J-A, Bassel-Duby R *et al.* Modulation of adverse cardiac remodeling by STARS, a mediator of MEF2 signaling and SRF activity. *J Clin Invest* 2007;**117**:1324–1334.
14. Pachucki J, Burmeister LA, Larsen PR. Thyroid hormone regulates hyperpolarization-activated cyclic nucleotide-gated channel (HCN2) mRNA in the rat heart. *Circ Res* 1999;**85**:498–503.
15. Yanagi K, Takano M, Narazaki G, Uosaki H, Hoshino T, Ishii T *et al.* HCN and Cav3 channels confer automaticity of embryonic stem-derived cardiomyocytes. *Stem Cells* 2007;**25**:2712–2719.
16. Jochum W, Passegue E, Wagner EF. AP-1 in mouse development and tumorigenesis. *Oncogene* 2001;**20**:2401–2412.
17. Lin Q, Schwarz J, Bucana C, Olson E-N. Control of mouse cardiac morphogenesis and myogenesis by transcription factor MEF2C. *Science* 1997;**276**:1404–1407.
18. Kim Y, Phan D, vanRooij E, Wang D-Z, McAnally J, Qi X *et al.* The MEF2D transcription factor mediates stress-dependent cardiac remodeling in mice. *J Clin Invest* 2008;**118**:124–132.
19. Naya F-J, Black B-L, Wu H, Bassel-Duby R, Richardson J-A, Hill J-A *et al.* Mitochondrial deficiency and cardiac sudden death in mice lacking MEF2A transcription factor. *Nat Med* 2002;**11**:1303–1309.
20. Zhao X-S, Gallardo T-D, Lin L, Schageman J-J, Shohet R-V. Transcriptional mapping and genomic analysis of the cardiac atria and ventricles. *Physiol Genomics* 2002;**12**:53–60.

OPEN ACCESS Freely available online PLoS GENETICS

Progressive Purkinje Cell Degeneration in *tambaleante* Mutant Mice Is a Consequence of a Missense Mutation in HERC1 E3 Ubiquitin Ligase

Tomoji Mashimo[1,2☯], Ouadah Hadjebi[3☯], Fabiola Amair-Pinedo[3], Toshiko Tsurumi[2], Francina Langa[1], Tadao Serikawa[2], Constantino Sotelo[4], Jean-Louis Guénet[1]*, Jose Luis Rosa[3]*

1 Département de Biologie du Développement, Institut Pasteur, Paris, France, **2** Institute of Laboratory Animals, Graduate School of Medicine, Kyoto University, Kyoto, Japan, **3** Departament de Ciències Fisiològiques II, IDIBELL, Campus de Bellvitge, Universitat de Barcelona, L'Hospitalet de Llobregat, Barcelona, Spain, **4** Cátedra de Neurobiología del Desarrollo "Remedios Caro Almela", Instituto de Neurociencias de Alicante, Universidad Miguel Hernández y CSIC, Alicante, Spain

Abstract

The *HERC* gene family encodes proteins with two characteristic domains: HECT and RCC1-like. Proteins with HECT domains have been described to function as ubiquitin ligases, and those that contain RCC1-like domains have been reported to function as GTPases regulators. These two activities are essential in a number of important cellular processes such as cell cycle, cell signaling, and membrane trafficking. Mutations affecting these domains have been found associated with retinitis pigmentosa, amyotrophic lateral sclerosis, and cancer. In humans, six *HERC* genes have been reported which encode two subgroups of HERC proteins: large (HERC1-2) and small (HERC3-6). The giant HERC1 protein was the first to be identified. It has been involved in membrane trafficking and cell proliferation/growth through its interactions with clathrin, M2-pyruvate kinase, and TSC2 proteins. Mutations affecting other members of the HERC family have been found to be associated with sterility and growth retardation. Here, we report the characterization of a recessive mutation named *tambaleante*, which causes progressive Purkinje cell degeneration leading to severe ataxia with reduced growth and lifespan in homozygous mice aged over two months. We mapped this mutation in mouse chromosome 9 and then performed positional cloning. We found a G⇔A transition at position 1448, causing a Gly to Glu substitution (Gly483Glu) in the highly conserved N-terminal RCC1-like domain of the HERC1 protein. Successful transgenic rescue, with either a mouse BAC containing the normal copy of *Herc1* or with the human *HERC1* cDNA, validated our findings. Histological and biochemical studies revealed extensive autophagy associated with an increase of the mutant protein level and a decrease of mTOR activity. Our observations concerning this first mutation in the *Herc1* gene contribute to the functional annotation of the encoded E3 ubiquitin ligase and underline the crucial and unexpected role of this protein in Purkinje cell physiology.

Citation: Mashimo T, Hadjebi O, Amair-Pinedo F, Tsurumi T, Langa F, et al. (2009) Progressive Purkinje Cell Degeneration in *tambaleante* Mutant Mice Is a Consequence of a Missense Mutation in HERC1 E3 Ubiquitin Ligase. PLoS Genet 5(12): e1000784. doi:10.1371/journal.pgen.1000784

Editor: Harry Orr, University of Minnesota, United States of America

Received July 20, 2009; **Accepted** November 23, 2009; **Published** December 24, 2009

Funding: This study was supported by grants from Spain (BFU-2004-06329/BMC, BFU-2007-65452/BMC, and BFU-2008-02084/BMC to JLR and SAF-2004-07990 to CS), European Union (FEDER), Generalitat de Catalunya (2009SGR00022), and Japan (No.17700378). OH and FAP are supported by IGSOC and Generalitat de Catalunya, respectively. The funders had no role in study design, data collection and analysis, decision to publish, or preparation of the manuscript.

Competing Interests: The authors have declared that no competing interests exist.

* E-mail: joseluisrosa@ub.edu (JLR); jlguenet@orange.fr (J-LG)

☯ These authors contributed equally to this work.

Introduction

The cerebellum plays the role of a coordination centre, integrating peripheral sensory information on movement and position of the body parts to fine-tune gait and balance. Structural or functional alterations of this part of the central nervous system result in a complex syndrome, called ataxia, which is characterized by neurological signs that are clinically obvious in most species including the mouse. Many such mutations, either of spontaneous origin or resulting from strategies of genetic engineering performed *in vitro*, have been studied in detail in this species that, synergistically with human studies, have allowed advancement of our understanding of the developmental mechanisms generating the uniquely complex mature cerebellum.

In this publication, we report the positional cloning of an autosomal recessive mouse mutation, called *tambaleante* (symbol *tbl*; meaning staggering in Spanish), which is precisely characterized by a severe ataxic syndrome [1,2]. Mice homozygous for this mutation (*tbl/tbl*) exhibit an unstable gait, abnormal hindlimb posture and tremor. All these phenotypic characteristics correlate with a progressive degeneration of Purkinje cells (PCs) starting by two months of age. *tbl* mice thus represent a model of recessively inherited ataxia with progressive neurodegeneration of PCs. Using a combination of genetic, histological and biochemical approaches, we have been able to characterize the pathology of this mutation that we could relate to a mutation in the gene encoding the E3 ubiquitin ligase HERC1.

Results

Characterization of the *tambaleante* mutation

The *tambaleante* (*tbl*) mutation arose spontaneously in the DW/JPas inbred substrain, at the Institut Pasteur, and appeared to be inherited as an autosomal recessive condition with complete

Author Summary

The cerebellum is a coordination center whose function is to fine-tune vertebrates' gait and balance; and for this reason, alterations or damage affecting this structure result in a complex syndrome, called ataxia, with neurological signs that are easily recognized. In the mouse, many mutations producing ataxia have been identified and characterized. They have contributed to a better understanding of the genetics of cerebellum development, physiology, and pathology. The present study identifies the recessive allele responsible for the progressive and massive degeneration of the Purkinje cells observed in mutant mice previously named *tambaleante*. The mutation leads to a single amino acid substitution in a highly conserved domain (RCC1-like) of the giant protein HERC1. This protein belongs to the families HECT (E3 ubiquitin ligases) and RCC1 (GTPases regulators). While a variety of mutations have been reported in several members of these families, leading to sterility, growth retardation, retinitis pigmentosa, amyotrophic lateral sclerosis, or cancer, no mutation had ever been reported so far in the mouse *Herc1* gene. This report demonstrates the crucial and unexpected role of HERC1 in Purkinje cell physiology that could be considered helpful in the development of new therapeutic strategies for neurodegenerative disorders.

penetrance. The most remarkable phenotypic feature of homozygous (*tbl/tbl*) mice was an unstable gait, with abnormal hind limb-clasping reflex, which became really obvious from two months of age and worsened with time (Figure 1A and Video S1). To quantify these observations, we performed rotarod assays with these animals. Figure 1B shows that *tbl* animals stayed less time on the rotarod without falling. To visualize the progressive degeneration of PC, we performed an analysis of cerebellum sections stained with haematoxylin and eosin (H&E). In Figure 1C–1F, we can observe the great loss of PC between 1–3 months in *tbl* animals. Immunostaining using anti-calbindin D28-k antibodies (Figure 1G–1J) of parasagital sections of mouse cortex of 4 month old shows that *tbl* mice is almost completely depleted of PC. Compared to their normal littermates, *tbl/tbl* homozygotes were smaller in size. Growth curves showed that the weight of the mutant animals was significantly and constantly lower than the weight of controls, varying from 15 to 30% according to age and gender (Figure 2). Mutant animals also showed a lower survival rate since less than 40 percent of the latter survived longer than 40 weeks on the original DW background (Figure 2). Both sexes appeared to be fertile although poor breeders.

Mapping and identification of the *tambaleante* mutation

Genotyping 30 F2 mutant offspring (60 meiotic events) of an inter-subspecific cross between DW-*tbl/tbl* males and wild type (+/+) females of the inbred strain MBT/Pas [3], allowed us to assign the locus for *tbl* to chromosome 9, within a 1.7 cM interval flanked by markers *D9Mit233* and *D9Mit165* (Figure 3A and 3B). Although this interval encompassed the locus of the staggerer (*Rora*^{sg}) mutation, which occurred in the gene encoding RAR-related orphan receptor alpha and is also characterized by a severe cell-autonomous defect of Purkinje cell [4], we could eliminate this gene as causative of the *tambaleante* phenotype through the finding and characterization of a recombination event between the loci for *tbl* and the one of *Rora* (Figure 3A). In addition, a complementation test performed by mating *tbl/tbl* mice to +/*Rora*^{sg} mice and yielding exclusively normal offspring confirmed non allelism of the two

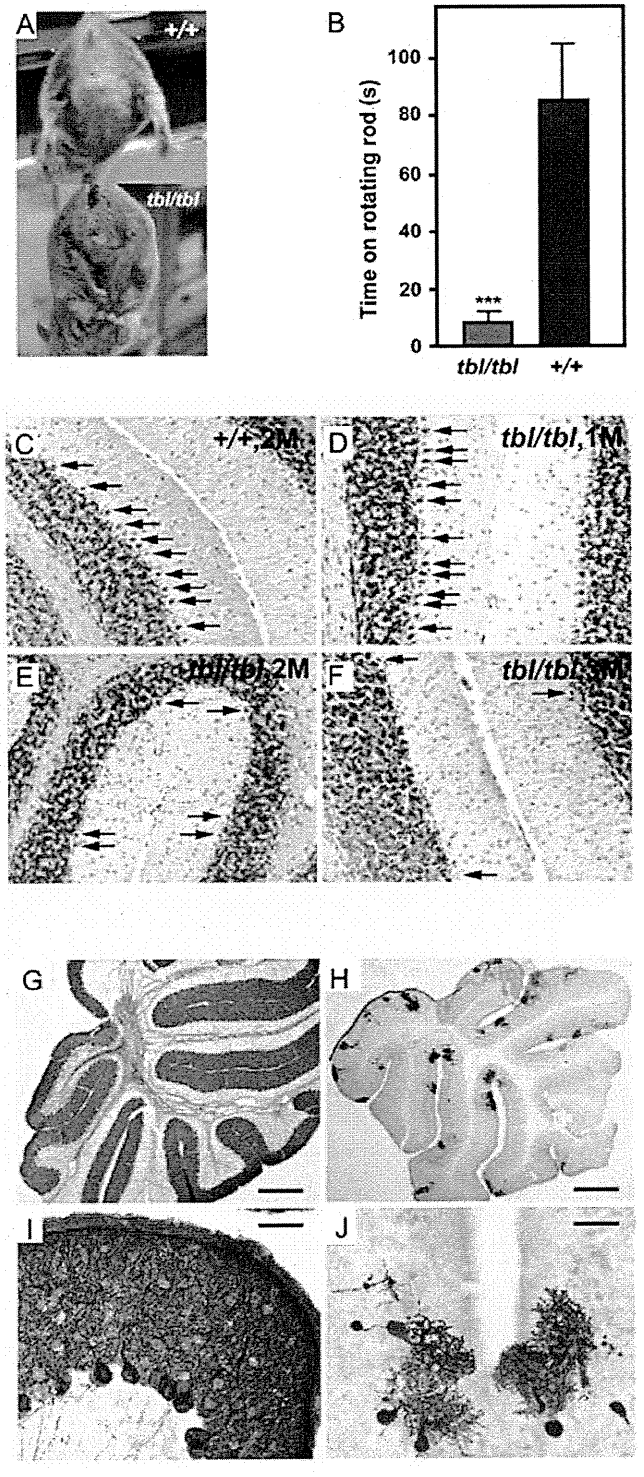

Figure 1. Characteristics of *tambaleante* mice. Hind limbs clasping reflex (A) and rotarod performance (B) of *tambaleante* (*tbl/tbl*) and control (+/+) mice. Data show mean±s.d. *** $p<0.001$ (C) H&E stained sections of the cerebellum of a +/+ control mouse aged two months. (D–F) H&E sections of the cerebellum of *Herc1*^{tbl}/*Herc1*^{tbl} mice aged respectively of 1, 2, and 3 months (M), exhibiting Purkinje cell degeneration. Anti-calbindin D28-k staining of parasagittal sections of a normal (G,I) and *tambaleante* (H,J) mouse cortex aged 4 months. The cortex of the mutant mouse is almost completely depleted of PCs. Scale bars: (G,H) 500 μm; (I,J) 25 μm.
doi:10.1371/journal.pgen.1000784.g001

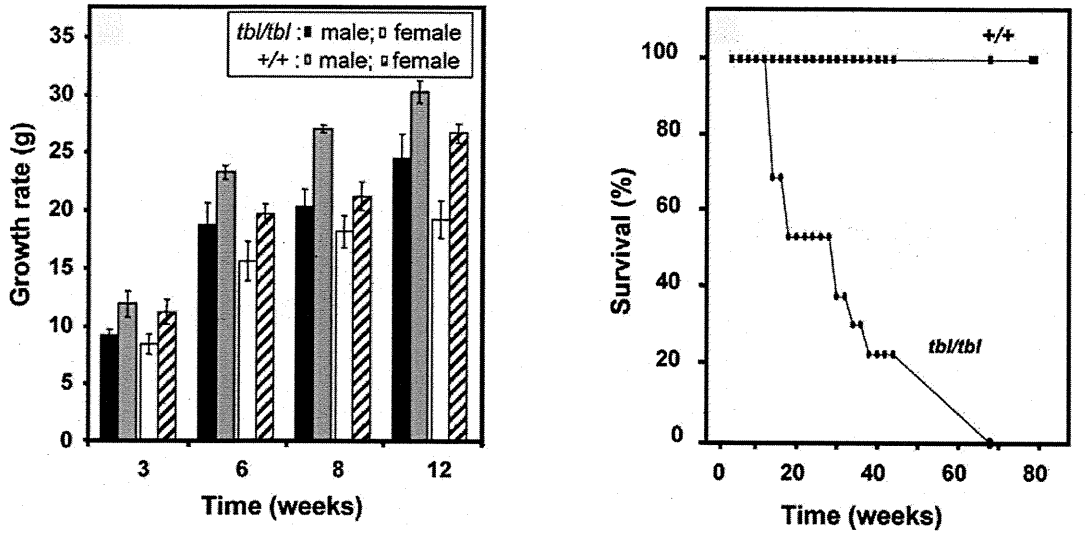

Figure 2. Growth and lifespan of *tambaleante* mice and control. Graphs of growth (left) and survival (right) from mice *tambaleante* (*tbl/tbl*) and mice control (+/+). Growth was analyzed in mice (n>9) aged 3–12 months of age. Data show mean±s.d.
doi:10.1371/journal.pgen.1000784.g002

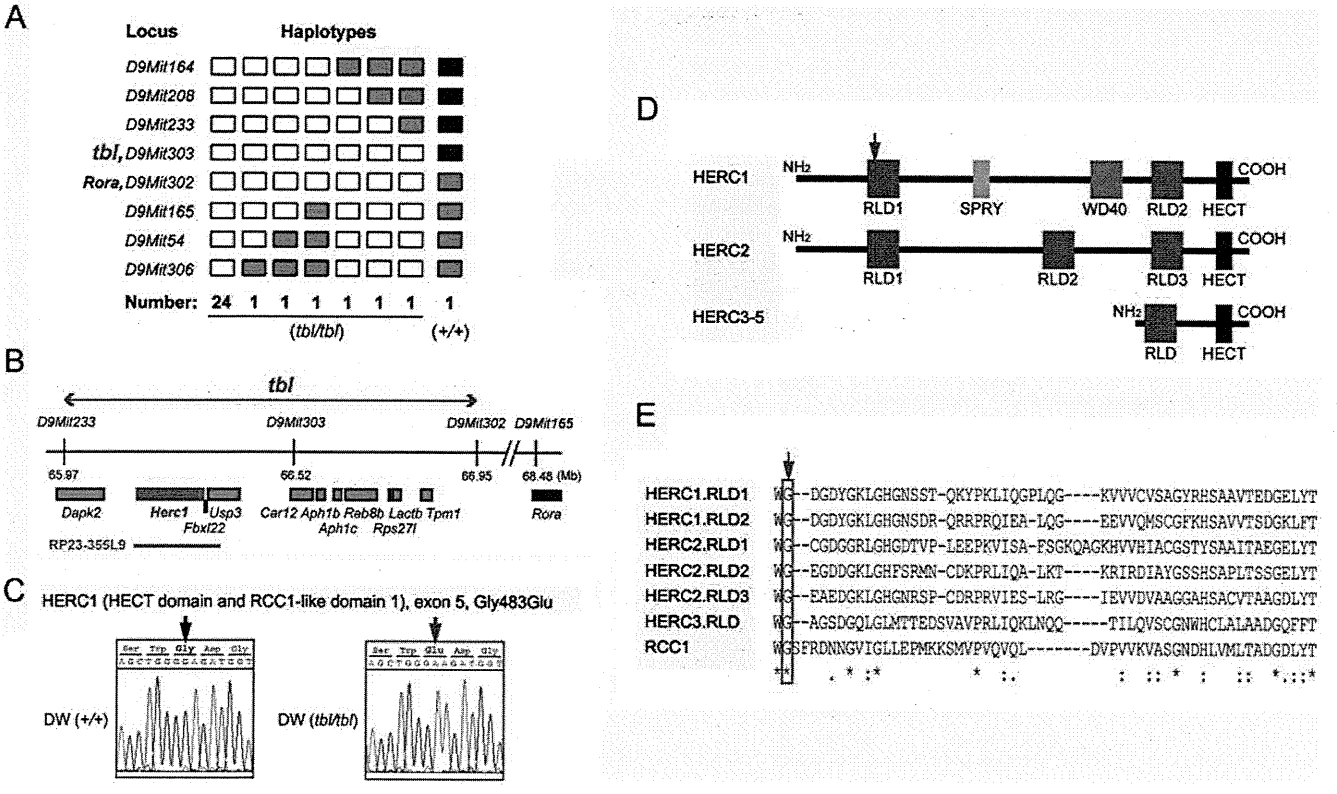

Figure 3. Molecular genetics of the *Herc1*^{tbl} locus. (A) Genotyping 30 *tbl/tbl*–F2 mice (60 meiotic events) of an intersubspecific cross allowed to map the *tbl* locus to mouse chromosome 9 between *D9Mit233* and *D9Mit165*. White rectangles symbolize homozygosity for the DW genotype, blue rectangles symbolize heterozygosity, and deep blue homozygosity for MBT genotype. A single mouse, with a crossover between *D9Mit302* and *D9Mit303* and a +/+ genotype at the *tbl* locus, allowed us to eliminate the *Rora* locus (where the mutation *staggerer* occurred) as a candidate. (B) The *tbl* candidate region contains eleven genes. BAC clone RP23-355L9 (shown as a green line) was used for transgenic rescue. (C) Sequence analysis of the cDNA from *Herc1*^{tbl}/*Herc1*^{tbl} and +/+ DW mice showed a point mutation in exon 5, resulting in a Gly⇔Glu substitution. This missense mutation is located in the RCC1-like domain (RLD) 1 of the HERC1 protein (arrow in D) and changes a highly preserved glycine in the HERC and RCC1 family of proteins (arrow in E; see also [11]). Mouse HERC family and characteristic domains are also shown (D; see text for details).
doi:10.1371/journal.pgen.1000784.g003

mutations (data not shown). Finally, the *tbl* candidate region was reduced to a genomic segment of 0.6 cM (~0.98 Mb) between *D9Mit233* (65.97 Mb) and *D9Mit302* (66.95 Mb), which contains eleven known genes as indicated in the *ENSEMBL* sequence database (http://www.ensembl.org/Mus_musculus) (Figure 3A and 3B). Among the eleven genes that were identified in the interval, three candidates (*Herc1*; *Usp3* and *Rab8b*) appeared top ranked considering their expression profile and the known or putative functions of the encoded proteins (Figure 3B). Among these three candidates, *Herc1* seemed to be the most likely one considering its large size and its sequence homology with *Herc2*, a locus where mutations that have phenotypes similar to *tambaleante* have already been reported [5,6]. Sequence analysis of the ~15 kb cDNA corresponding to this gene and comparison with the sequences of the co-isogenic strain DW, allowed to identify a single nucleotide difference (a G1448A transition at ENSMUST00000042824) between the *tbl* and the normal (+) haplotype that resulted in a Gly483Glu substitution (Figure 3C). Sequence comparison with several other unrelated inbred strains confirmed that this sequence alteration was recent and unique to the mutant haplotype. The G⇔A transition in the *tambaleante* haplotype generated a new restriction site for the *MboII* enzyme that allowed us to design a PCR assay, helpful for the diagnostic of *tbl* haplotype by discriminating +/+ from +/*tbl* or *tbl*/*tbl* (Figure 4).

Rescue of *tambaleante* phenotype

To ascertain that the Gly483Glu substitution identified in *Herc1* was really causative of the abnormal phenotype observed in *tbl*/*tbl* mice, we decided to attempt the rescue of the *tambaleante* phenotype by crossing *tbl*/*tbl* mice with transgenic mice expressing a normal copy of the *Herc1* gene. We used two strategies to generate such transgenic mice: in the first case we used the mouse BAC clone RP23-355L9 (~160 kb - encompassing the *Herc1* locus and a gene encoding a leucine-rich repeat protein 22 (*Fbxl22*) that is not expressed in the brain [7] (Figure 3B)); then we used the human cDNA of *HERC1* (96% amino acid identity with mouse) [8]. BAC transgenic ($Tg^{RP23\text{-}355L9}$/+) mice were crossed with heterozygous (+/*tbl*) mice, then the F1 mice were mated with heterozygous (+/*tbl*) mice to obtain *tbl* homozygous mice with the transgenic copies (*tbl*/*tbl*; $Tg^{RP23\text{-}355L9}$/+). We found that the phenotype of these mice was greatly improved since none of the animals exhibited the phenotypic characteristics of *tambaleante* mutants during the period they were observed (as an example see footprint experiments in Figure S1). By 3 months of age, PCs in these transgenic mice remained normal at least in number and size, indicating complete phenotypic rescue (Figure S1). Complete transgenic rescue was also achieved with the other transgenic strain generated from the human *HERC1* cDNA [6] in pCI-*neo* ($Tg^{HERC1cDNA}$) (Figure S2). The complete phenotypic rescue was also analyzed by weight, rotarod performance, cerebellar staining with H&E and immunohistochemistry with anti-calbindin D28-k antibodies (Figure 5). No differences in the parameters analyzed were observed between wild-type animals and transgenic mice. From these results we considered that the pathology in *tambaleante* mice is indeed a direct consequence of the molecular defect in *Herc1*. For this reason, we use $Herc1^{tbl}$ as an official symbol for the *Herc1* mutant allele.

Expression of the *Herc1* gene and functional analysis

Analysis of the *Herc1* gene expression by Northern blotting has been previously reported and revealed ubiquitous expression in mammalian tissues although at very low levels in the liver [8]. We have confirmed these data by RT-PCR in mouse tissues using specific primers for *Herc1* (Figure 6). *In situ* hybridization of brain sections also confirmed a pattern similar to that shown in the Allen Brain Atlas [9, and data not shown].

The HERC proteins have a HECT (Homologous to E6-AP COOH-terminus) domain and at least one domain related with RCC1 (Regulator of Chromosome Condensation 1). HECT domains are involved in the transfer of ubiquitin or ubiquitin-like proteins to target substrates. RCC1-like domains (RLD) seem more versatile and may have a role in guanine nucleotide exchange on small GTP-binding proteins, in enzyme inhibition and in interaction with proteins and lipids. Proteins containing

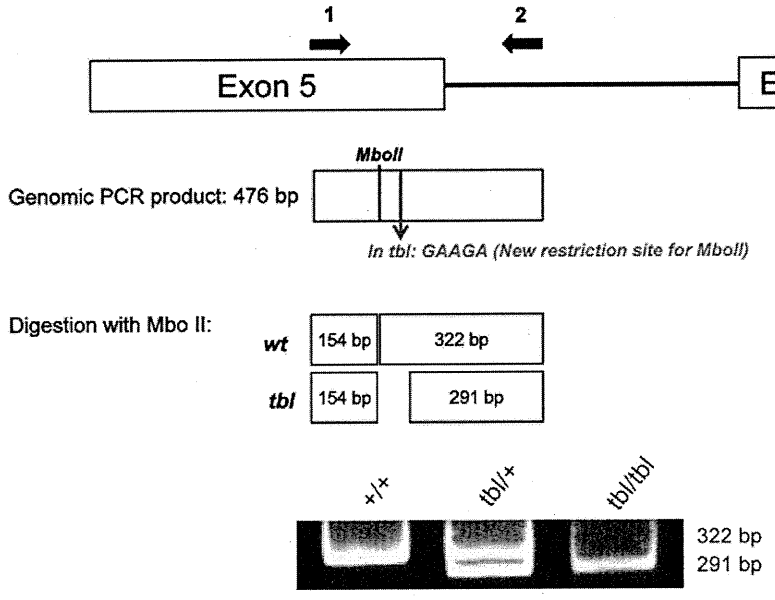

Figure 4. Genotyping analysis of *tbl* mutation. The *tbl* mutation generates a new restriction site (GAAGA) for the *Mbo*II enzyme. PCR amplification of genomic DNA samples of wild-type (+) or $Herc1^{tbl}$ haplotypes with specific primers followed by digestion of the amplification products with the *Mbo*II enzyme allows identifying a haplotype specific pattern by PAGE.
doi:10.1371/journal.pgen.1000784.g004

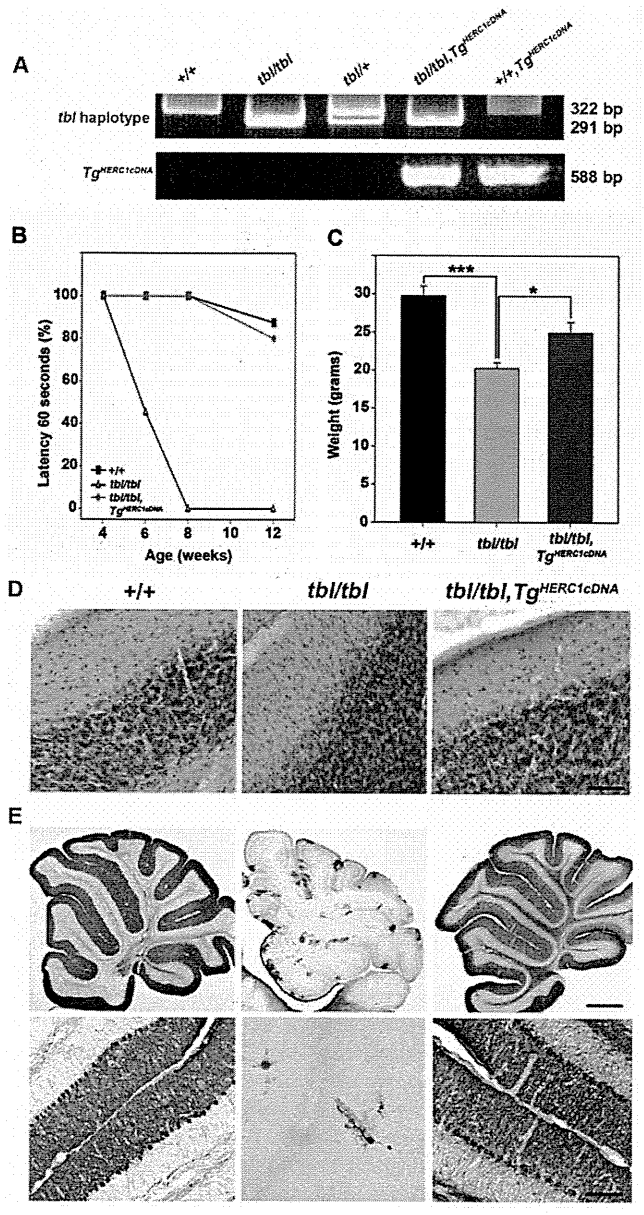

Figure 5. Rescue of the *tambaleante* phenotype. (A) Genotyping analysis by PCR of genomic DNA to identify transgenic and *tambaleante* animals. (B) Motor coordination was tested in wild-type (+/+), homozygous (*tbl/tbl*), and homozygous with transgenic copies (*tbl/tbl;Tg*^{HERC1cDNA}) animals (n = 5–9). Testing began at 4 weeks of age and was conducted until week 12 to follow the progression on each phenotype. The animals were put on the rotarod until the latency to fall off reached the total time of 60 s and the percentatge (%) of animals that stayed during this time was represented. (C) Weight chart of these animals (n = 5–9) aged 3–6 months of age. Data show mean ± s.d. *** $p<0.001$, * $p<0.05$. Staining with H&E (D) and immunostaining with anti-calbindin D28k antibodies (E) of cerebellum sections of these animals. Scale bars: (D,E lower pictures) 25μm; (E upper pictures) 500μm. See Materials and Methods for detailed protocols.
doi:10.1371/journal.pgen.1000784.g005

some of these domains are important regulators of cellular processes such as cell cycle, cell signalling and membrane trafficking. HERC1 protein was the first protein of this family to be identified. It contains one HECT domain, two RLD (RLD1 and RLD2), seven WD40 repeats and one SPRY domain (Figure 3D and 3E) [10–12]. The Gly483Glu substitution found in *tambaleante* mice is located within the highly conserved N-terminal RCC1-like domain (RLD1) of the HERC1 protein and presumably alters its structure and function (Figure 3D and 3E) [10]. To check whether *Herc1*^{tbl} mutation affected the HERC1 protein levels, we performed Western-blot analysis using anti-HERC1 antibodies with samples from brain, cerebellum and kidney of mice older than 3 months. Surprisingly, we observed a significant increase in the amount of HERC1 protein in mutant mice, suggesting a possible increase of its stability (Figure 7A and 7D). No changes were observed with any other protein such as clathrin heavy chain (CHC) that was used as loading control (Figure 7A). Similar results were also found in skeletal muscle (not shown).

HERC1 has been previously reported to interact with TSC2 protein. *TSC1* and *TSC2* are tumour-suppressor genes that are mutated in the tumour syndrome TSC (tuberous sclerosis complex). Their gene products form the TSC1-TSC2 complex (also named hamartin-tuberin complex) and, through its GAP (GTPase-activating protein) activity towards the small G-protein Rheb (Ras homolog enriched in brain), this complex is a negative regulator of mTORC1 (mammalian target of rapamycin complex 1) [13]. Because processes such as growth, autophagy and neuronal plasticity are known to be regulated, at least in part, through the mTOR pathway [14,15] and because *Herc1*^{tbl}/*Herc1*^{tbl} mice show features related to these processes (neuronal degeneration and smaller size), we hypothesized that a mutant HERC1 protein might affect some of these events through deregulation of the mTOR pathway. With this guess in mind, we first analyzed whether the levels of the TSC1-TSC2 complex and mTOR protein were modified in the brain of *Herc1*^{tbl}/*Herc1*^{tbl} mice. We found that the levels of these proteins remained normal in these animals suggesting that the mutant HERC1 protein does not affect their stability (Figure 7B). We then checked whether the mTOR activity was modified, and to achieve this, we analyzed the phosphorylation of a substrate of the mTORC1 activity, the ribosomal protein S6 kinase 1 (S6K1). We observed a decrease of the phosphorylation of S6K1 at threonine 389 (P-T389-S6K1) in brain of *Herc1*^{tbl}/*Herc1*^{tbl} mutant mice (Figure 7C). These data were also confirmed and quantified in kidney where P-T389-S6K1 levels were found higher compared to +/+ mice (Figure 7C).

Because it had been previously reported that mTOR negatively regulates autophagy [16], we thought that the decrease of the mTORC1 kinase activity could correlate with an increase of autophagy in *tbl/tbl* mice. The conversion of the microtubule-associated protein light chain 3 (LC3-I) to its phosphatidylethanolamine-modified form (LC3-II) has been used as marker of the accumulation of autophagosomes [17]. We have measured by immunoblot analysis this autophagy marker observing an increase of LC3-II levels in brain and cerebellum of *tambaleante* mice (Figure 7B and 7C). To check that this increase was due to increases in autophagic activity and not to reduced turnover of autophagosomes [18], we also measured the steady-state levels of the known substrate for autophagy p62/SQSTM1 [19]. We observed a significant decrease in the steady-state levels of p62/SQSTM1 (Figure 7C) indicating that autophagic flux was not blocked. Altogether these data suggest that autophagy is induced in *tbl/tbl* mice. An attractive hypothesis would be that this activation is the cause of PC death in the *tambaleante* mice. This however is difficult to ascertain because an increase in autophagy is also a protective mechanism for cells in response to stressing stimuli. To determine whether this was the case or not, we analyzed the occurrence of autophagy at an earlier phase of the PC degeneration; in 2-month-old *Herc1*^{tbl}/*Herc1*^{tbl} cerebellum. Double labeling with antibodies against anti-calbindin D28-k and

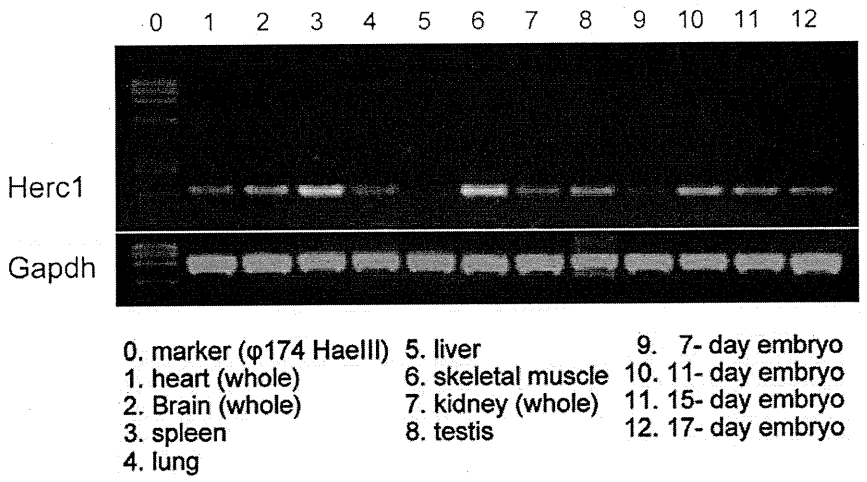

Figure 6. *Herc1* gene expression in mice. *Herc1* is widely expressed in various tissues as indicated by RT–PCR. *Gapdh* expression was used as control.
doi:10.1371/journal.pgen.1000784.g006

lysosome-associated membrane protein LAMP-1 allowed us to identify lysosomes with large cytoplasmic accumulations in dendrites and somata being particularly numerous in regions of the cerebellar cortex which had lost the calbindin D28-k expression (Figure 7E). Electron microscopy also performed on 2-month-old mice showed that PC bodies contained numerous autophagosomes (vacuoles with double membrane and filled with cytoplasmic organelles) and autolysosomes (vacuoles with a single membrane and filled with larger inclusions) (Figure 7F–7H). Altogether these data show that activation of autophagy in $Herc1^{tbl}/Herc1^{tbl}$ mutant mice is indeed the earliest pathological process that seems to be involved in the degeneration and death of PCs. This high degree of autophagy is unique to the $Herc1^{tbl}$ mutation and has never been reported before for any other cerebellar mutation [20].

Discussion

Genes of the *Herc/HERC* family are absent in prokaryotes and in eukaryotes such as fungi and plants. In mammalian genomes there are several *HERC* paralogous copies encoding two subgroups of proteins: large (HERC1–2) and small (HERC3–6 in human; HERC3–5 in mouse). The HERC1 giant protein, which was the first to be identified in a screening looking for human oncogenes, contains several domains (one HECT, two RLDs, seven WD40 repeats and one SPRY) involved in protein ubiquitilation, guanine nucleotide exchange and protein-protein or protein-lipid interaction. This structure probably reflects the multiple interactions of this protein with other cellular proteins. HERC1 interacts with phosphoinositides and with several other proteins such as clathrin, ADP-ribosylation factor (ARF), M2-pyruvate kinase and TSC2 and, through these interactions it has been involved in membrane trafficking, cell growth and proliferation [8,10–12].

The Gly483Glu substitution that we found in *tambaleante* mice, which is located within the highly conserved RLD1 domain (Figure 3D–3E), presumably alters the structure of the HERC1 protein and very likely impairs its functions as well [10–11]. The structural alteration might be causative of an increase in its stability, leading to the observation of an unexpected increased level of this protein in all studied tissues (Figure 7A, 7B, and 7D). Impairment of HERC1 function through the mTOR pathway could explain the neuronal degeneration and the smaller size observed in *tambaleante* mice. Since mTOR has been reported to be a negative regulator of autophagy [16], a decrease of its activity would indeed correlate with an increase of autophagy observed in the PCs of *tambaleante* mice (Figure 7). Although future studies are required to understand the precise role of HERC1, we can however conclude that HERC1 has a profound impact in the animal growth and the maintenance of the cerebellum structure.

A consensus is emerging among molecular geneticists stressing that a missense mutation, affecting only one site of a multidomain protein, is sometimes of better value for gene annotation than a knockout allele that, in general, suppresses at once the protein. In the case of $Herc1^{tbl}$ the situation may be more complex. If the Gly483Glu amino acid substitution has an effect on the protein structure, then one may expect heterozygous mice to be affected to some extent. This however does not seem to be the case since, as far as we could observe from those $Herc1^{tbl}/+$ breeders that we kept for more than one year, we never noticed any symptoms in their gait or behaviour that would have been evocative of a pathology of the central nervous system (CNS). We did not conduct any observation at the histological level on these mice but it is not sure that this would have been of great value if we consider that a decrease in PCs number seems to be a common observation in mice heterozygous for most mutations affecting the cerebellum (*nr*, $Rora^{sg}$, $Agtpbp1^{pcd}$ and $Reln^{rl}$) [20]. It does not appear that the $Herc1^{tbl}$ mutation has a dominant negative effect on the HERC1 function because transgenic mice could rescue the *tambaleante* phenotype. Our data seem to indicate that the *tambaleante* protein is not functional or has acquired a different function to the wild-type protein and that the presence of wild-type protein has a dominant effect. For this reason, heterozygous or rescued mice, where the wild-type HERC1 protein is present, do not exhibit a *tambaleante* phenotype.

Because ataxia is the most apparent feature in *tambaleante* mice and because this symptom is commonly associated to a cerebellar defect, we focused more on this part of the CNS than on any other in our morphological survey. However, in all cases, the paraffin embedding and serial sectioning after Nissl staining that were achieved on adult mutant CNS, did not allow detection of any obvious lesion outside the cerebellum (retina was not analyzed). Nevertheless, the possibility that some type of alteration could be disclosed using more specialized methods (immunohistochemistry, electron microscopy) remains open.

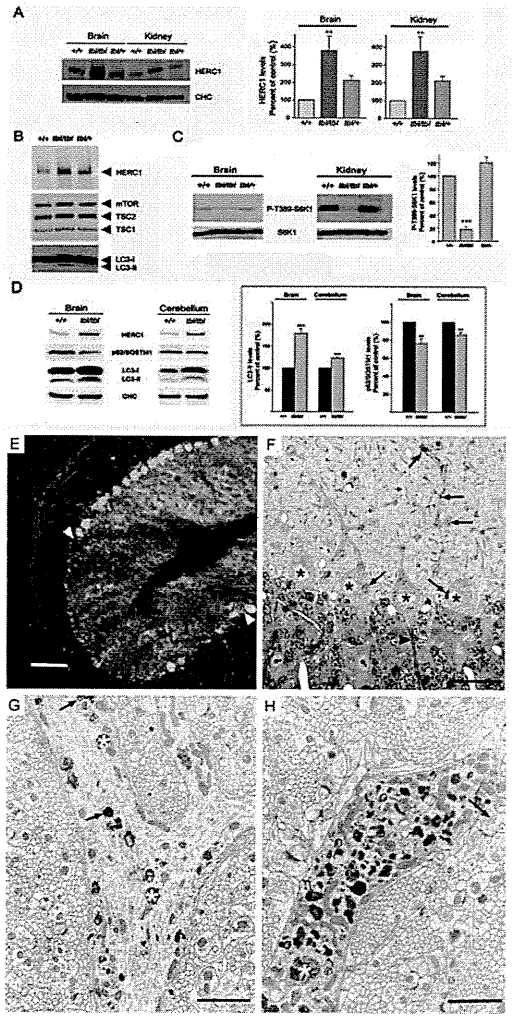

Figure 7. *Herc1* expression and functional analysis. Brain (A–D), kidney (A,C) and cerebellum (D) homogenates from wild-type (+/+), heterozygous (+/*tbl*) and homozygous (*tbl/tbl*) mice were analyzed by Western-blot using specific antibodies against the indicated proteins. HERC1 (in brain and in kidney), P-T389-S6K1 (in kidney), p62/SQSTM1 and LC3-II (in brain and in cerebellum) levels were quantified (n = 4–9) and expressed as the mean±s.d. of percentage of respective control. ** $p<0.01$,*** $p<0.001$. (E) Parasagittal section of a 2-month-old *tbl/tbl* cerebellum double immunostained with anti-calbindin D28k antibodies to visualize PC (green) and anti-LAMP-1 (red) to identify lysosomes and autophagosomes. The arrowheads point to an area of the cerebellar cortex almost devoid of PC. In this area, LAMP-1 positive puncta are numerous, testifying for the degeneration of PC. (F) Parasagittal 1µm-thick plastic section stained with toluidine blue, illustrating four PC somata (asterisks). The arrows point to dense cytoplasmic inclusions accumulated in the cell bodies and proximal dendrites, particularly at their branching points. The arrowhead points to the first Ranvier node of a PC axon initial segment, which looks normal. (G,H) Electron-micrographs made from the same mouse showing two profiles of the proximal dendritic compartment. The one in (G) illustrates a branching zone in an early stage of the autophagic process. The dendrite contains some vacuoles bound by a smooth double membrane (arrows), enclosing whorls of membrane-like elements, and dense debris (asterisks) suspended in an electronlucent matrix. The other dendritic profile (H) corresponds to a more advanced stage in autophagy, characterized by the occurrence of extremely numerous single membrane bound vacuoles corresponding to autolysosomes, some of them of large size (asterisk). The arrow points to a giant spine emerging from the dendrite and postsynaptic to several parallel fibers varicosities. *Scale bars*: the bar is equal to 100 µm in (E), 24 µm in (F), 1.2 µm in (G), and 1.5 µm in (H).
doi:10.1371/journal.pgen.1000784.g007

In humans, genes encoding proteins with mutations in their RCC1 domains have been found to be involved in several diseases [11]. The best studied is probably the *RPGR* (Retinitis pigmentosa GTPase regulator) gene, which is responsible for 70–80% of the most severe forms of human the X-linked retinitis pigmentosa [16], and in which more than 200 independent mutations have been identified. Functional studies suggest a role for this protein in microtubule-dependent transport along cilia [21]. Another example is provided by the *ALS2* (amyotrophic lateral sclerosis 2-juvenile) locus, which encodes for a protein where mutations have been associated to an autosomal recessive form of juvenile-onset amyotrophic lateral sclerosis (jALS) [22,23]. All mutations found in this gene lead to the production of truncated proteins. Interestingly, truncations affecting its amino-terminus, where the RCC1-like domain is located, lead to jALS with degeneration of upper and lower spinal cord motorneurons, whereas less severe truncations in the protein Alsin lead only to degeneration of the upper motorneurons [24,25]. Gene expression of HERC1 has also been reported to be increased in human tumour cell lines [8] and decreased in heroin users with a genetic variation of the opioid receptor [26].

HERC2, the other member of the large HERC family, has also been found associated with pathologies. Mutations in the mouse *Herc2* gene were found to be responsible for the so-called *runty, jerky, sterile*-syndrome or, in short, *rjs*-syndrome, also known as *jdf-2 (juvenile development and fertility-2)* [5,6]. The pathogenic mechanisms of this syndrome are not known at the molecular level, but it has been suggested that at least some of its symptoms could be due to pituitary defects. In humans, the *HERC2* genomic locus, including several partially duplicated paralogs (duplicons) of *HERC2* [27,28], corresponds to the chromosomal breakpoint region in deletions that cause the Prader-Willi and Angelman syndromes [29,30] although lack of HERC2 protein does not seem to play a role in these syndromes [6]. Recently, it has been reported that a single nucleotide polymorphism in intron 86 of the *HERC2* gene determines human blue/brown eye colour by controlling the expression of the neighboring gene *OCA2* [31–33].

In summary, the present study unambiguously demonstrates that the gene *Herc1* is involved in the mutation *tambaleante* and shows, for the first time, that this gene has a profound impact on growth and maintenance of the cerebellar structure. To our knowledge, no other mutant allele has ever been reported at the *Herc1* locus before *Herc1*^{tbl}. Considering the relative great size of this gene (78 exons - with a predicted coding region of 14,559 bp) this is rather surprising and probably means that a majority of the mutations likely to occur at this locus either have no deleterious effects or, most probably, that they are lethal *in utero* and accordingly remained undetected so far. This is an important difference with the *Herc2* locus where at least a dozen mutations have been reported that lead to the *rjs/jdf2* syndrome [5,6]. This also means that, in spite of ancestral relationships, the two proteins have acquired some specific, non-redundant functions.

Materials and Methods

Animals

The *tambaleante* mutation is available at the RIKEN BioResource Center, Tsukuba, Japan (<http://www2.brc.riken.jp/> - Ref: RBRC00188). The mouse strain transgenic for the mouse BAC clone RP23-355L9 was generated in Kyoto University by direct *in ovo* injection. The mouse strain transgenic for the full-length human *HERC1* cDNA was generated at the Institute Pasteur. The transgene was previously generated in two steps: first, we digested pCIneo vector (The vector carries the cytomegalovirus

(CMV) immediate-early enhancer/promoter, from Promega) with the restriction enzyme *BglII* and ligated the annealed oligonucleotide GATCTATCGATA generating a new *ClaI* restriction site in pCIneo vector. Then the full-length human *HERC1* cDNA [8] was cloned into this modified pCIneo (pJLR189). The transgene cassette was linearized by *Cla*I, purified by agarose gel and microinjected *in ovo*. All animal experiments were performed following European and Japanese institutional guidelines for animal handling and research.

Genotyping

Tail DNA samples were prepared from mice according to [34] and PCR amplification of the exon containing the *tambaleante* mutation was performed using the primers: 5′-GCTTGTGGTAAAGGCAGCTATGGG-3′ and 5′-CCTCACATGTCCCCACACAC-3′, yielding a 476 bp product (PCR settings were: 94°C×5 minutes, 94°C×30 seconds, then annealing at 60°C for 30 seconds, and elongation at 72°C for 30 seconds. Number of cycles: 35). Amplification products were then digested with *Mbo*II enzyme and fractionated in a 10% PAGE to distinguish among *tbl/+*, *tbl/tbl* and +/+ mice. Transgenic mice were PCR-genotyped using the primers: 5′-TGGTGGAAATAGTATCCCAC-3′ and 5′-CACGGTCAGTAGTCAGTGTC-3′, yielding a 588 bp product (PCR settings: 94°C×5 minutes, 94°C×30 seconds, then annealing at 55°C for 30 seconds, and elongation at 72°C for 45 seconds. Number of cycles: 35).

RT–PCR

A mouse multiple-tissue and embryo cDNA set (Mouse MTC Panel I, Clontech) was used for expression analysis of *Herc1* gene. RT-PCR was performed with following primers: 5′-GAAGATGTGGATGCAGCAGA-3′ and 5′- GGTCTGTCCGGTGAAGGATA-3′ for mouse *Herc1* cDNA (199 bp), and *Gapdh* 5′ and 3′ PCR primers (983 bp) as a control. To assess transgene expression, total RNA was isolated from mouse brains using the Ultraspec RNA Isolation System (Biotecx). 2 µg of total RNA were reverse-transcribed using the cDNA Reverse Transcription kit (Applied Biosystems) and random primers. PCR was carried out with primers: 5′-AGTCGACTGGATCCGGTACC-3′ and 5′-AGTCTGGCAACTGTGGTCCT-3′ for the transgene and 5′-ATGGATGACGATATCGCTG-3′ and 5′-ATGAGGTAGTCCGTCAGGA-3′ for the actin control.

Histology and immunohistochemistry

Mice were perfused transcardially with a fixative containing 4% formaldehyde in 0.1 M phosphate buffer after being deeply anesthetized by diethyl ether inhalation. The cerebellum was removed and postfixed in the same fixative for two hours, then embedded in gelatin 8% and subsequently processed for respective histological analyses. Tissue samples were stored at −80°C and cut on a cryostat. Cryosections were stained with H&E or immunostained with rabbit polyclonal anti-calbindin D28k or anti-LAMP-1 antibodies. For immunostaining, the cerebellum was processed according to [35].

Neurobehavioural assays

The rotarod test was used to assess motor coordination and function (rotarod apparatus: ROTAROD/RS Panlab; diameter: 3.5 cm, length: 5 cm). For Figure 5, three groups were constituted: +/+ (n = 8, four males, four females), *tbl/tbl* (n = 9, four males, five females), *tbl/tbl* $Tg^{HERC1cDNA}$ (n = 5, two males, three females). Testing began at 4 weeks of age and was conducted until week 12 to follow the progression on each phenotype. In brief, animals were trained a constant speed (16 rpm) for 60 s. The animals were put on the rotarod until the latency to fall off reached the total time of 60 s. Each mouse was placed on the rotarod with its head in the direction of rotation and so had to turn to the opposite direction. We performed three trials per day with 2–6 min intervals, on three consecutive days. During the pauses between the turns, mice were allowed to rest in their home cages. After training, mice were evaluated once at 6, 8 and 12 weeks of age at a constant speed of 12 rpm until the latency of fall reached 1 min. The percentage (%) of animals that stayed for 60s is shown in Figure 5. For Figure 1, each mouse had three trials per test with an intertrial interval of 5 minutes. Mice (n = 4 to 9) were placed on the rotating drum at 20 rpm and the time the animal stayed on the rotarod without falling off was measured. The hind limb clasping reflex was assessed by holding the mouse by its tail for 30 seconds.

Antibodies used

Horseradish peroxidase-coupled secondary antibodies (Molecular Probes); anti-mTOR and anti-P-T389-S6K1 (1A5) antibodies (Cell Signalling Technology); anti-TSC2 (C-20), anti-S6K1 (C-18) and anti-LAMP-1 (N-19) antibodies (Santa Cruz Biotechnology, Inc.); anti-CHC antibody (BD Transduction laboratories); anti-HERC1 antibodies [8]; anti-LC3 antibody (MBL); anti-calbindin D28k antibody (Swant, Bellinzona, Switzerland); anti-p62/SQSTM1 antibody (Abnova).

Lysates and immunoblotting

Mice (3–7 months old) were euthanized by cervical dislocation. Organs were collected and frozen in liquid nitrogen and stored at −80°C until analysis. Tissues were prepared in lysis buffer (consisting of 10 mM Tris-HCl, pH 7.5, 100 mM NaCl, 1.5 mM $MgCl_2$, 50 mM NaF, 1 mM sodium vanadate, 1 mM phenylmethylsulfonyl fluoride, 5 mg/ml leupeptin, 5 mg/ml aprotinin, 1 mg/ml pepstatin A, 50 mM β-glycerophosphate, 100 mg/ml benzamidine), homogenized in a motor-driven Polytron PT3000 (Kinematica AG) incubated in a precooled tube with CHAPS 0.3% for 20 minutes, and centrifuged at 13,500g for 15 min at 4°C. Total protein levels were measured by BCA (Pierce). Equal amounts of supernatant proteins (200µg/lane) were separated by electrophoresis. To analyze simultaneously in the same SDS/PAGE gel giant proteins such as HERC1 or mTOR and small proteins such as LC3, lysates were loaded in a combination of SDS/PAGE gels named LAG gel [36]. After running the gel overnight, the proteins were transferred to PVDF membranes and visualized by immunoblotting using specific antibodies as previously described [36]. Band intensities were analyzed with a gel documentation system (LAS-3000 Fujifilm). The protein levels were normalized with respect to CHC, mTOR or S6K1 levels and expressed as percentage of controls.

Supporting Information

Figure S1 Rescue of the *tambaleante* phenotype with $Tg^{RP23\text{-}355L9}$. Foot prints (A,B) and H&E staining of cerebellar sections (C,D) of *tbl/tbl* mice (A,C) and *tbl/tbl* mice transgenic for BAC RP23-355L9 at 12-weeks-old.
Found at: doi:doi:10.1371/journal.pgen.1000784.s001 (0.34 MB TIF)

Figure S2 Expression of the transgene $Tg^{HERC1cDNA}$. Total RNA was isolated from mouse brains (*tbl/tbl*; $Tg^{HERC1cDNA}$/+; *tbl/tbl*;$Tg^{HERC1cDNA}$/+). 2 µg of total RNA were reverse-transcribed using random primers. PCR was carried with specific primers for transgene and actin. Actin was used as control. Transgene cassette (pJLR189) was used as positive control and pDEST-HA vector as

negative control. Amplified DNA was run in agarose gels stained with ethidium bromide.
Found at: doi:doi:10.1371/journal.pgen.1000784.s002 (0.23 MB TIF)

Video S1 Tambaleante mouse. A 30-second video of a two-month-old *tambaleante* (*tbl/tbl*) male mouse.
Found at: doi:doi:10.1371/journal.pgen.1000784.s003 (3.18 MB AVI)

Acknowledgments

We thank T. Kuramoto, F. R. Garcia-Gonzalo, E. Casas-Terradellas, I. Tato, F. Ventura, R. Bartrons, S. Alcantara, J. Llorens, J. Chubbocks, and A. Gimeno for support and comments.

Author Contributions

Conceived and designed the experiments: TM OH TS CS JLG JLR. Performed the experiments: TM OH FAP TT FL CS JLR. Analyzed the data: TM OH FAP TT FL TS CS JLG JLR. Contributed reagents/materials/analysis tools: TM OH TS CS JLG JLR. Wrote the paper: TM OH FAP CS JLG JLR.

References

1. Wassef M, Sotelo C, Cholley B, Brehier A, Thomasset M (1987) Cerebellar mutations affecting the postnatal survival of Purkinje cells in the mouse disclose a longitudinal pattern of differentially sensitive cells. Dev Biol 124: 379–389.
2. Rossi F, Jankovski A, Sotelo C (1995) Target neuron controls the integrity of afferent axon phenotype: a study on the Purkinje cell-climbing fiber system in cerebellar mutant mice. J Neurosci 15: 2040–2056.
3. Bonhomme F, Guénet JL (1996) The laboratory mouse and its wild relatives. In: Lyon MF, Rastan S, Brown SDM, eds. Genetic Variants and Strains of the Laboratory Mouse, 3rd edn. Oxford: Oxford University Press. pp 1577–1596.
4. Hamilton BA, Frankel WN, Kerrebrock AW, Hawkins TL, FitzHugh W, et al. (1996) Disruption of the nuclear hormone receptor RORalpha in staggerer mice. Nature 379: 736–739.
5. Lehman AL, Nakatsu Y, Ching A, Bronson RT, Oakey RJ, et al. (1998) A very large protein with diverse functional motifs is deficient in rjs (runty, jerky, sterile) mice. Proc Natl Acad Sci U S A 95: 9436–9441.
6. Ji Y, Walkowicz MJ, Buiting K, Johnson DK, Tarvin RE, et al. (1999) The ancestral gene for transcribed, low-copy repeats in the Prader-Willi/Angelman region encodes a large protein implicated in protein trafficking, which is deficient in mice with neuromuscular and spermiogenic abnormalities. Hum Mol Genet 8: 533–542.
7. Ilyin GP, Rialland M, Glaise D, Guguen-Guillouzo C (1999) Identification of a novel Skp2-like mammalian protein containing F-box and leucine-rich repeats. FEBS Lett 459: 75–79.
8. Rosa JL, Casaroli-Marano RP, Buckler AJ, Vilaró S, Barbacid M (1996) p619, a giant protein related to the chromosome condensation regulator RCC1, stimulates guanine nucleotide exchange on ARF1 and Rab proteins. EMBO J 15: 4262–4273.
9. Lein ES, Hawrylycz MJ, Ao N, Ayres M, Bensinger A, et al. (2007) Genome-wide atlas of gene expression in the adult mouse brain. Nature 445: 168–176.
10. Garcia-Gonzalo FR, Rosa JL (2005) The HERC proteins: functional and evolutionary insights. Cell Mol Life Sci 62: 1826–1838.
11. Hadjebi O, Casas-Terradellas E, Garcia-Gonzalo FR, Rosa JL (2008) The RCC1 superfamily: from genes, to function, to disease. Biochim Biophys Acta 1783: 1467–1479.
12. Rotin D, Kumar S (2009) Physiological functions of the HECT family of ubiquitin ligases. Cell 10: 398–409.
13. Chong-Kopera H, Inoki K, Li Y, Zhu T, Garcia-Gonzalo FR, et al. (2006) TSC1 stabilizes TSC2 by inhibiting the interaction between TSC2 and the HERC1 ubiquitin ligase. J Biol Chem 281: 8313–8316.
14. Wullschleger S, Loewith R, Hall MN (2006) TOR signalling in growth and metabolism. Cell 124: 471–484.
15. Huang J, Manning BD (2008) The TSC1-TSC2 complex: a molecular switchboard controlling cell growth. Biochem J 412: 179–190.
16. Inoki K, Corradetti MN, Guan KL (2005) Dysregulation of the TSC-mTOR pathway in human disease. Nat Genet 37: 19–24.
17. Kabeya Y, Mizushima N, Ueno T, Yamamoto A, Kirisako T, et al. (2000) LC3, a mammalian homologue of yeast Apg8p, is localized in autophagosome membranes after processing. EMBO J 19: 5720–5728.
18. Klionsky DJ, Abeliovich H, Agostinis P, Agrawal DK, Aliev G, et al. (2008) Guidelines for the use and interpretation of assays for monitoring autophagy in higher eukaryotes. Autophagy 16: 151–175.
19. Bjørkøy G, Lamark T, Pankiv S, Øvervatn A, Brech A, et al. (2009) Monitoring autophagic degradation of p62/SQSTM1. Methods Enzymol 452: 181–197.
20. Dusart I, Guénet JL, Sotelo C (2006) Purkinje cell death: Differences between developmental cell death and neurodegenerative death in mutant mice. Cerebellum 5: 163–173.
21. Shu X, Black GC, Rice JM, Hart-Holden N, Jones A, et al. (2007) RPGR mutation analysis and disease: an update. Hum Mutat 28: 322–328.
22. Hadano S, Hand CK, Osuga H, Yanagisawa Y, Otomo A, et al. (2001) A gene encoding a putative GTPase regulator is mutated in familial amyotrophic lateral sclerosis 2. Nat Genet 29: 166–173.
23. Yang Y, Hentati A, Deng HX, Dabbagh O, Sasaki T, et al. (2001) The gene encoding alsin, a protein with three guanine-nucleotide exchange factor domains, is mutated in a form of recessive amyotrophic lateral sclerosis. Nat Genet 29: 160–165.
24. Gros-Louis F, Gaspar C, Rouleau GA (2006) Genetics of familial and sporadic amyotrophic lateral sclerosis. Biochim Biophys Acta 1762: 956–972.
25. Chandran J, Ding J, Cai H (2007) Alsin and the molecular pathways of amyotrophic lateral sclerosis. Mol Neurobiol 36: 224–231.
26. Drakenberg K, Nikoshkov A, Horváth MC, Fagergren P, Gharibyan A, et al. (2006) Mu opioid receptor A118G polymorphism in association with striatal opioid neuropeptide gene expression in heroin abusers. Proc Natl Acad Sci U S A 103: 7883–7888.
27. Ji Y, Rebert NA, Joslin JM, Higgins MJ, Schultz RA, et al. (2000) Structure of the highly conserved HERC2 gene and of multiple partially duplicated paralogs in human. Genome Res 10: 319–329.
28. Chai JH, Locke DP, Greally JM, Knoll JH, Ohta T, et al. (2003) Identification of four highly conserved genes between breakpoint hotspots BP1 and BP2 of the Prader-Willi/Angelman syndromes deletion region that have undergone evolutionary transposition mediated by flanking duplicons. Am J Hum Genet 73: 898–925.
29. Amos-Landgraf JM, Ji Y, Gottlieb W, Depinet T, Wandstrat AE, et al. (1999) Chromosome breakage in the Prader-Willi and Angelman syndromes involves recombination between large, transcribed repeats at proximal and distal breakpoints. Am J Hum Genet 65: 370–386.
30. Nicholls RD, Knepper JL (2001) Genome organization, function, and imprinting in Prader-Willi and Angelman syndromes. Ann Rev Genomics Hum Genet 2: 153–175.
31. Sturm RA, Duffy DL, Zhao ZZ, Leite FP, Stark MS, et al. (2008) A single SNP in an evolutionary conserved region within intron 86 of the HERC2 gene determines human blue-brown eye color. Am J Hum Genet 82: 424–431.
32. Kayser M, Liu F, Janssens AC, Rivadeneira F, Lao O, et al. (2008) Three genome-wide association studies and a linkage analysis identify HERC2 as a human iris color gene. Am J Hum Genet 82: 411–423.
33. Eiberg H, Troelsen J, Nielsen M, Mikkelsen A, Mengel-From J, et al. (2008) Blue eye color in humans may be caused by a perfectly associated founder mutation in a regulatory element located within the HERC2 gene inhibiting OCA2 expression. Hum Genet 123: 177–187.
34. Beermann F, Hummler E, Schmid E, Schütz G (1993) Perinatal activation of a tyrosine aminotransferase fusion gene does not occur in albino lethal mice. Mech Dev 42: 59–65.
35. Alcántara S, Pozas E, Ibañez CF, Soriano E (2006) BDNF-modulated spatial organization of Cajal-Retzius and GABAergic neurons in the marginal zone plays a role in the development of cortical organization. Cereb Cortex 16: 487–499.
36. Casas-Terradellas E, Garcia-Gonzalo FR, Hadjebi O, Bartrons R, Ventura F, et al. (2006) Simultaneous electrophoretic analysis of proteins of very high and low molecular weights using low-percentage acrylamide gel and a gradient SDS-PAGE gel. Electrophoresis 27: 3935–3938.

Cancer Science
The official journal of the Japanese Cancer Association

Enhanced colitis-associated colon carcinogenesis in a novel *Apc* mutant rat

Kazuto Yoshimi,[1] Takuji Tanaka,[2] Akiko Takizawa,[1] Megumi Kato,[3] Masumi Hirabayashi,[3] Tomoji Mashimo,[1] Tadao Serikawa[1] and Takashi Kuramoto[1,4]

[1]Institute of Laboratory Animals, Graduate School of Medicine, Kyoto University, Yoshidakonoe-cho, Sakyo-ku, Kyoto; [2]Department of Oncologic Pathology, Kanazawa Medical University, Uchinada, Ishikawa; [3]National Institute for Physiological Sciences, The Graduate University for Advanced Studies, Okazaki, Japan

(Received May 18, 2009/Revised June 28, 2009/Online publication August 20, 2009)

To establish an efficient rat model for colitis-associated colorectal cancer, azoxymethane and dextran sodium sulfate (AOM/DSS)-induced colon carcinogenesis was applied to a novel adenomatous polyposis coli (*Apc*) mutant, the Kyoto Apc Delta (KAD) rat. The KAD rat was derived from ethylnitrosourea mutagenesis and harbors a nonsense mutation in the *Apc* gene (S2523X). The truncated APC of the KAD rat was deduced to lack part of the basic domain, an EB1-binding domain, and a PDZ domain, but retained an intact β-catenin binding region. KAD rats, homozygous for the *Apc* mutation on a genetic background of the F344 rat, showed no spontaneous tumors in the gastrointestinal tract. At 5 weeks of age, male KAD rats were given a single subcutaneous administration of AOM (20 mg/kg, bodyweight). One week later, they were given DSS (2% in drinking water) for 1 week. At week 15, the incidence and multiplicity of colon tumors developed in the KAD rat were remarkably severe compared with those in the F344 rat: 100 versus 50% in incidence and 10.7 ± 3.5 versus 0.8 ± 1.0 in multiplicity. KAD tumors were dominantly distributed in the rectum and distal colon, resembling human colorectal cancer. Accumulation of β-catenin protein and frequent β-catenin mutations were prominent features of KAD colon tumors. To our knowledge, AOM/DSS-induced colon carcinogenesis using the KAD rat is the most efficient to induce colon tumors in the rat, and therefore would be available as an excellent model for human colitis-associated CRC. (*Cancer Sci* 2009; 100: 2022–2027)

Colorectal cancer (CRC) is one of the leading causes of cancer deaths in the world. Globally, the CRC mortality was 639 000 in 2004.[1] Chronic inflammation has been identified as a potential risk factor for CRC. Clinical studies have shown that inflammatory bowel disease, such as Crohn's disease[2] and ulcerative colitis,[3] elevates the risk of CRC.

Animal experiments are assumed to simulate or at least provide plausible pathophysiological mechanisms of various diseases, including cancer and chronic inflammatory disorders. For inflammation-related CRC, a two-stage colitis-related mouse colon carcinogenesis model was recently established.[4] In this model, colon carcinogenesis is initiated with carcinogens and then dextran sodium sulfate (DSS), which can induce colonic mucosal inflammation resembling the histopathology of ulcerative colitis, is used as a tumor-promoting agent. Colon carcinogenesis initiated with carcinogens such as azoxymethane (AOM),[4] 1,2-dimethylhydrazine (DMH),[5] and heterocyclic amines[6] is effectively promoted in combination with DSS.

The two-stage colitis-related model has been applied to a rat colon carcinogenesis study. Similar to mice, DSS also promotes DMH-induced[7] and AOM-induced[8]colon carcinogenesis in the F344 rat. These rat models can be utilized to investigate the pathogenesis of colitis-related colon carcinogenesis and to detect carcinogenesis modifiers.[7,8] For more effective colorectal carcinogenesis, however, a novel model, in which much more and larger tumors are induced in a shorter experiment period, is required. It would be preferable to obtain a large volume of tumors, sufficient to be identifiable on macroscopic observation, because this would be an advantage in testing chemotherapeutic efficacy of anticancer drugs as well as chemoprevention ability of anti-inflammatory drugs.

One possible idea to enhance the AOM/DSS model is deficiency of the tumor suppressor adenomatous polyposis coli (*Apc*) gene, which plays a significant role in tumor development in the gut,[9] for example, AOM enhances colorectal carcinogenesis in $Apc^{min/+}$ mice that carry a germline mutation in the *Apc* gene and develop multiple polyps in the intestine.[10] Furthermore, DSS strongly promotes colorectal carcinogenesis in $Apc^{min/+}$ mice.[11] These findings prompted us to examine AOM/DSS-induced colon carcinogenesis in an *Apc* mutant rat. In the rat, an *Apc*-deficient Pirc rat is available.[12] The Pirc rat carries a nonsense mutation in the *Apc* gene and the resultant truncated APC (Δ1137) lacks the β-catenin binding region. The Pirc rat develops multiple tumors with a distribution between the colon and small intestine. The average number of colonic polyps is 8 ± 3 in Pirc rats aged 4–6 months, and most of them are adenomas. *N*-ethyl-*N*-nitrosourea (ENU) treatment enhances colonic polyps, but it takes more than 7 months to obtain them.[12] However, a carcinogenesis test with AOM alone or AOM/DSS has not yet been done in the Pirc rats.

We have recently produced a rat mutant archive consisting of cryopreserved sperm derived from ~5000 ENU-mutagenized male rats and corresponding DNA samples. The mutant archive is estimated to store ~2 million mutations, sufficient to find several mutations in a particular gene of interest.[13]

We present here a novel homozygous *Apc* mutant rat strain, the Kyoto Apc Delta (KAD) rat, from the rat ENU-mutant archive. KAD rats harbor a nonsense mutation in exon 15 that results in premature termination at codon 2523 of the serine residue of APC protein. KAD rats are viable and show no spontaneous tumors in the small intestine or colorectum. Treatment with AOM/DSS revealed an increased susceptibility of KAD rats to colitis-associated colon carcinogenesis in a 15-week experimental period. Also, the development of colorectal tumors can be tracked by endoscopic observation. AOM/DSS-induced colon carcinogenesis in the KAD rats will provide a novel rat model for investigating colitis-related colon carcinogenesis, identifying xenobiotics with modifying effects, and evaluating anticancer drug candidates.

Materials and Methods

Establishment of KAD rat strain. A total of 1735 DNA samples from ENU-mutagenized F344/NSlc rats from the Kyoto

[4]To whom correspondence should be addressed.
E-mail: tkuramot@anim.med.kyoto-u.ac.jp

doi: 10.1111/j.1349-7006.2009.01287.x

University Rat Mutant Archive (KURMA) were screened with seven sets of primers (Table S1). These primers were designed to amplify exons 9, 11, 14, or 15 of the rat *Apc* gene. Approximately 6.27 Mb of genomic DNA was screened. Rats carrying the *Apc* mutation were recovered by intracytoplasmic sperm injection.[13] Male rats carrying the *Apc* mutation were backcrossed five times with female F344/NSlc rats to remove latent mutations induced by ENU.

Western blotting. Proteins were prepared from the brainstems of KAD and control F344/NSlc rats at 5 weeks of age. Western blotting and signal detection were carried out as described.[14] Antibodies against the N terminus of APC (H-290; Santa Cruz Biotechnology, Santa Cruz, CA, USA), the C terminus of APC (C-20; Santa Cruz Biotechnology), and β-actin (AC-40; Sigma-Aldrich Japan, Tokyo, Japan) were used. Secondary antibodies against rabbit IgG (NA934; GE Healthcare Bio-Sciences, Tokyo, Japan) and mouse IgG (NA931; GE Healthcare Bio-Sciences) were used.

Carcinogenesis test. Colon carcinogenic tests were carried out as described.[4] Briefly, male KAD rats (n = 17) were divided into three experimental and control groups. Group 1 (n = 6) was given a single subcutaneous injection of AOM (20 mg/kg bodyweight) at 5 weeks of age. Starting 1 week after the AOM injection, animals were given 2% DSS in drinking water for 7 days and then no further treatment for 13 weeks. Groups 2 (n = 5) and 3 (n = 3) were given AOM alone and DSS alone, respectively. Group 4 (n = 3) was untreated. Male F344/NSlc rats (n = 6) were treated with AOM followed by DSS (group 5) and were controls of group 1. All rats were maintained under the conditions of humidity (50 ± 10%), light (14 : 10 h L : D cycle), and temperature (24 ± 2°C) at the Institute of Laboratory Animals, Graduate School of Medicine, Kyoto University. At 15 weeks after the AOM injection, they were killed by cervical dislocation under anesthesia with isoflurane (Forane; Abbott Japan, Tokyo, Japan). All experimental procedures were approved by the Animal Research Committee of Kyoto University and were carried out according to the Regulation on Animal Experimentation at Kyoto University.

Histopathology and immunohistochemistry. At autopsy, the colorectum of the rats was resected, washed with PBS, and opened longitudinally along the main axis. After careful macroscopic inspection, tumors and the colonic mucosa were dissected and processed for histopathological examination with hematoxylin–eosin staining. Immunohistochemical staining of β-catenin was carried out as described previously.[15]

Endoscopic observation and biopsy. Endoscopic observations were carried out every week after the 8 weeks of the carcinogenesis tests. Anesthesia was administrated through the regulated flow of isoflurane vapor (2%) through a nose cone. The colon was flushed with a tap water enema. The endoscope (BF TYPE 3C40; Olympus, Tokyo, Japan) was inserted into the colon and endoscopic images were acquired. A tumor specimen was biopsied under microscopic observation.

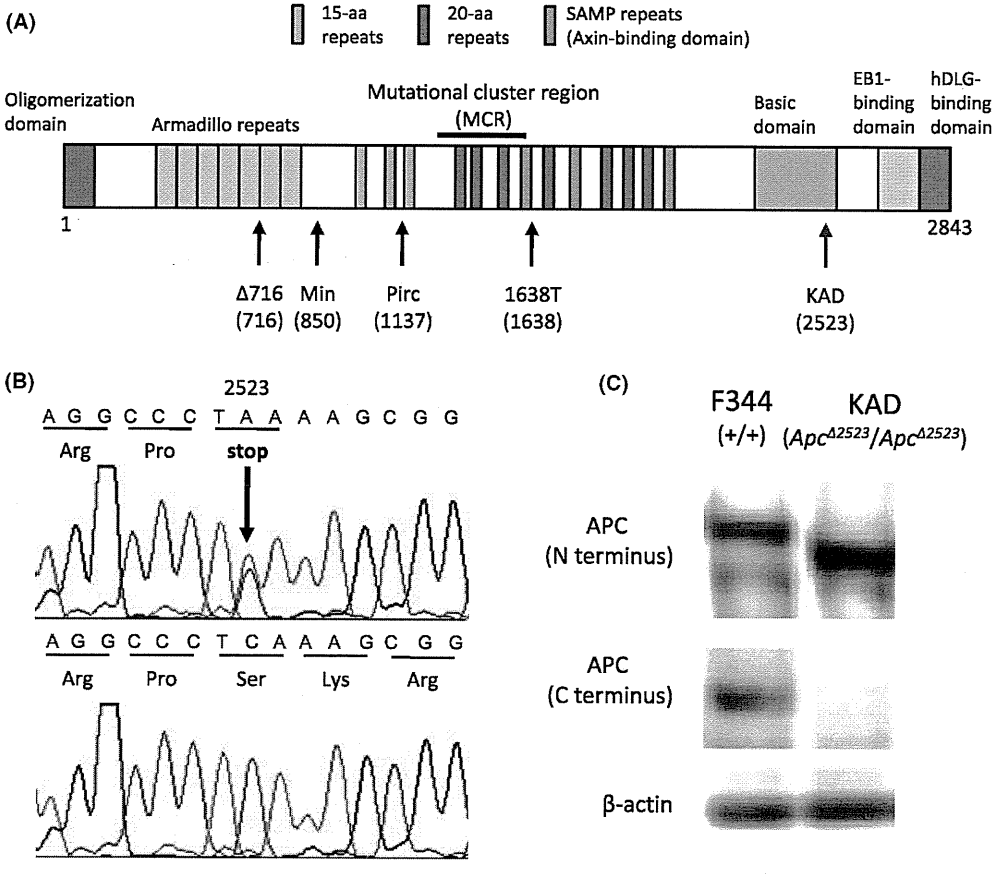

Fig. 1. Establishment of the Kyoto Apc Delta (KAD) rat strain. (A) Schematic diagram that shows multiple domains of full-length adenomatous polyposis coli (APC). Black arrows indicate orthologous locations of truncating mutations in mouse and rat models. The nonsense mutation in the KAD rat is indicated by a red arrow. (B) Sequence trace of a founder rat showing heterozygosity for C-to-A transversion (arrow) at nucleotide 7621 of the *Apc* gene (upper) compared with wild-type littermates (lower). The mutation generated a premature stop codon (TAA) at the 2523 amino acid position of APC. (C) Western blot analysis of APC in KAD and control F344/NSlc rats. Proteins extracted from the brains of F344 (+/+) and KAD ($Apc^{\Delta 2523}/Apc^{\Delta 2523}$) rats were hybridized with anti-N terminus of APC (top), anti-C terminus of APC (middle) antibodies. β-Actin was used as an internal control (bottom). In KAD rats, smaller APC protein was detected with the anti-N terminus APC antibody than F344 rats, and no signal was detected with the anti-C terminus APC antibody.

Mutation detection. Mutations of the β-catenin (*Catnnb1*) or K-ras (*Kras*) genes in tumors were screened by direct sequencing. Genomic DNA was extracted from tissues stored in RNAlater (Applied Biosystems, Inc., Carlsbad, CA, USA). PCR primers were designed to amplify mutational hot spots detected in the AOM-induced colon tumors.[16] The nucleotide sequences of primers were as follows: rCatnnb1-F, GCTGACCTCATGGAGTTGGA and rCatnnb1-R, GCTACTTGCTCTTGCGTGAA; rKras-F, TGAATTCAGAATGCCTTAGAGTTTT and rKras-R, GCACCGATGGTTCCCTATTA. DNA sequencing was carried out as described previously.[17]

Results

Establishment of the KAD rat. A C-to-A point mutation was detected in the DNA archive of KURMA and was predicted to result in premature termination at codon 2523 of the serine residue of the APC protein (Fig. 1A). Rats carrying the mutation were recovered from the corresponding frozen sperm (KURMA sperm archive number: ENU1588) with intracytoplasmic sperm injection.[13] The nonsense mutation (c. 7621C > A, p. Ser2523X) was confirmed in recovered animals, which were F_1 hybrids between recipient F344/NSlc and G_1 donor animals (Fig. 1B); we therefore named this allele $Apc^{\Delta 2523}$. The deduced APC protein was predicted to lack a part of the basic domain, EB1-binding domain, and PDZ domain (Fig. 1A). Because homozygous Min mice and Pirc rats have been reported to be embryonic lethal,[12,18] we crossed $Apc^{\Delta 2523}$ heterozygous mutants to obtain $Apc^{\Delta 2523}$ homozygotes. Rats homozygous for $Apc^{\Delta 2523}$ were viable and survived almost 2 years. We thus designated the $Apc^{\Delta 2523}$ homozygous strain the KAD rat. Western blot analyses indicated a lack of the C terminus of APC protein in the KAD rat (Fig. 1C). Cellular localization of β-catenin protein was not altered in the colon epithelia of the KAD rat, compared with the F344 rat (data not shown).

High susceptibility to colitis-associated colon carcinogenesis in the KAD rat. $Apc^{\Delta 2523}$ homozygous KAD developed no spontaneous tumors in their gastrointestinal tracts even after 20 months of age. We then tried to induce colon tumors in the KAD rats by administrating AOM as a chemical colonic carcinogen and/or DSS as a colitis-inducing agent. The AOM-treated (group 2), DSS-treated (group 3), and non-treated (group 4) KAD rats showed no colon tumors on either macroscopic or microscopic observation. Meanwhile, AOM/DSS-treated KAD rats (group 1) developed multiple colon tumors, of which the incidence, number, and volume could be compared with those of tumors developed in AOM/DSS-treated F344 rats (group 5). Interestingly, the AOM/DSS-treated KAD rats showed a higher incidence of diarrhea than the AOM/DSS-treated F344 rats during a few weeks after the cessation of DSS treatment (Fig. 2).

Macroscopically, all of the AOM/DSS-treated KAD rats showed multiple nodular, polypoid, or caterpillar-like colonic tumors (Fig. 3A), whereas half of the AOM/DSS-treated F344 rats had a few colonic tumors (Fig. 3B). The average number of colorectal tumors in the KAD rat was significantly higher than that of F344 rats (9.5 ± 1.8 vs 1.3 ± 0.8, $P < 0.0001$) (Fig. 4A). The average volume of KAD tumors was not different from that of F344 tumors (33.9 ± 23.0 mm^3 vs 10.3 ± 13.7 mm^3, $P = 0.38$). Colon tumors that developed in the KAD rats that received AOM and DSS were distributed more prominently in the rectum (4.0 ± 1.5) and distal colon (5.2 ± 1.7) than in the middle colon (0.3 ± 0.5) (Fig. 4B). No tumors were observed in the proximal colon, cecum, or small intestine.

Microscopically, tumors induced in AOM/DSS-treated KAD rats were diagnosed as tubular adenoma (Fig. 5A), well or moderately differentiated tubular adenocarcinoma (Fig. 5B), or signet-ring cell carcinoma (Fig. S1). The multiplicity of adenoma of the KAD rat was significantly higher than that of the F344 rat

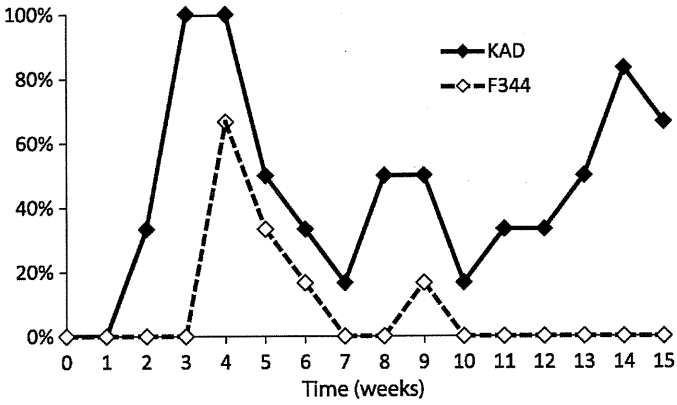

Fig. 2. Incidences of diarrhea observed in azoxymethane (AOM)/dextran sodium sulfate (DSS)-treated Kyoto Apc Delta (KAD) and F344 rats. Percentages of rats showing diarrhea in weekly observations are shown. One-week DSS administration is indicated by a grey box. Note that all KAD rats showed diarrhea in week 3, whereas no F344 rats showed diarrhea.

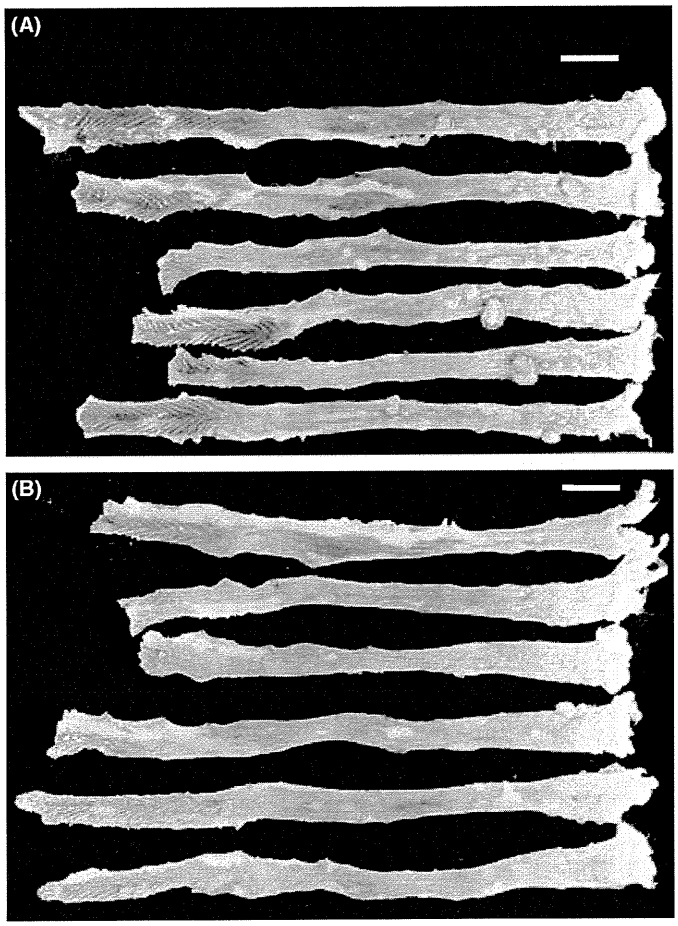

Fig. 3. Macroscopic view of large bowels of azoxymethane (AOM)/dextran sodium sulfate (DSS)-treated (A) Kyoto Apc Delta (KAD) and (B) F344 rats. Scale bars = 2 cm.

(7.7 ± 2.9 vs 0.3 ± 0.5, $P < 0.005$) (Fig. 4C). The multiplicity of adenocarcinoma of the KAD rat was also significantly higher than that of the F344 rat (3.0 ± 0.9 vs 0.5 ± 0.8, $P < 0.001$) (Fig. 4C). Twenty-two of 64 colon tumors induced in the KAD rats invaded the submucosa, muscularis propria, or serosa

doi: 10.1111/j.1349-7006.2009.01287.x

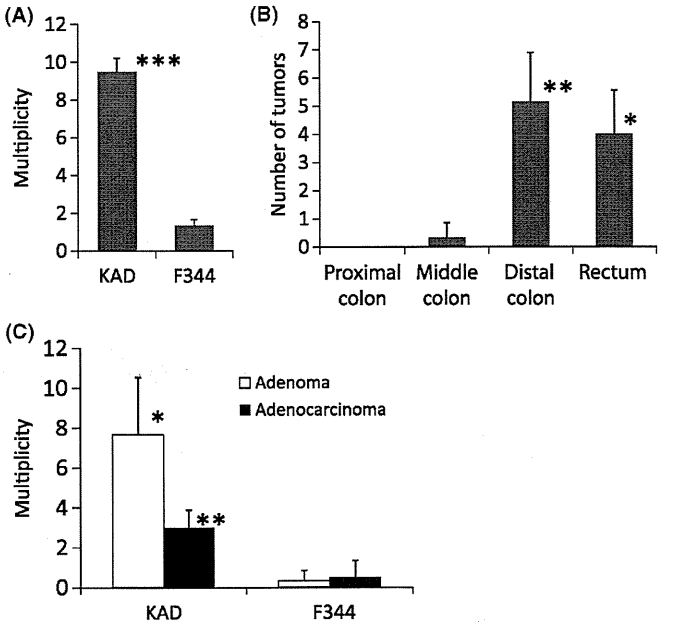

Fig. 4. Increased induction of colon tumors in azoxymethane (AOM)/dextran sodium sulfate (DSS)-treated Kyoto Apc Delta (KAD) rats. (A) Multiplicity of tumors observed macroscopically (mean ± SD) at week 15. ***$P < 0.0001$. (B) Distribution of colon tumors in AOM/DSS-treated KAD rats (mean ± SD) at week 15. **Distal colon versus middle colon, $P < 0.001$; *rectum versus middle colon, $P < 0.005$. (C) Multiplicities of adenoma and adenocarcinoma developed in KAD rats were significantly higher than in F344 rats at week 15. *$P < 0.005$, **$P < 0.001$.

(Fig. 5C), whereas none of the five colon tumors in F344 rats invaded the submucosa or deeper. Four signet-ring cell carcinomas were observed in the KAD rats. Apart from colonic tumors, colonic dysplasia was observed in all of the rats in groups 1 and 5. The average number of dysplasias in the KAD rats (11.2 ± 8.0) was greater than that of the F344 rats (3.7 ± 4.1), but the difference was insignificant ($P = 0.069$). No dysplastic lesions developed in groups 2–4.

Altered cellular localization of β-catenin protein is frequently observed in AOM- or AOM/DSS-induced colorectal tumors.[4,16] Strong β-catenin expression was seen in the cytoplasm and/or nucleus of adenoma and adenocarcinoma cells (Fig. 5D), which indicated the activation of Wnt signaling in these cells.

Endoscopic observation and biopsy of colon tumors. Endoscopic examination was done in the anesthetized KAD rats to determine whether the development of colorectal tumors can be observed without necropsy. We could observe colorectal lesions displaying differences from normal mucosa, including polypoid lesions, as early as the eighth week after AOM administration (Fig. S2A) and could monitor the development of both the number and volume of them during the carcinogenesis test (Fig. S2B). At week 8, the average number of lesions detected by endoscopy was 3.3 ± 1.2. The number of lesions gradually increased with the experimental period and reached 17.3 ± 4.5 at week 14, which was much higher than that of macroscopic observations. Such a discrepancy might be caused by the disappearance of inflammatory polyps at week 14. The biopsy of a tumor specimen under endoscopic observation was successful and the specimen was diagnosed histopathologically (Fig. S2C).

Highly frequent mutations of the β-catenin gene but no mutation of the K-ras gene in colon tumors. Mutation of the β-catenin gene in its glycogen synthase kinase (GSK) 3β phosphorylation consensus motif and K-ras mutation at codon 12 are features of AOM-induced rat colon tumors.[15,16] Direct sequencing of PCR products revealed 29 missense mutations in 29 of 39 (74.4%) colon tumors induced by AOM/DSS in KAD rats (Table 1). The mutation spectrum detected in the present study was quite similar to that detected in the AOM-induced rat colon tumors,[16] which indicated that a common molecular pathway to initiate colon carcinogenesis was shared in AOM- and AOM/DSS-treated colons. Meanwhile, no K-ras mutation at codon 12 was detected in the 39 colon tumors.

Discussion

A two-stage colitis-related colon carcinogenesis model provides a powerful tool for the induction of colon tumors in rats.[7,8] In the current study, to establish a more efficient colon carcinogenesis model, we produced a novel *Apc*-mutant KAD rat. The

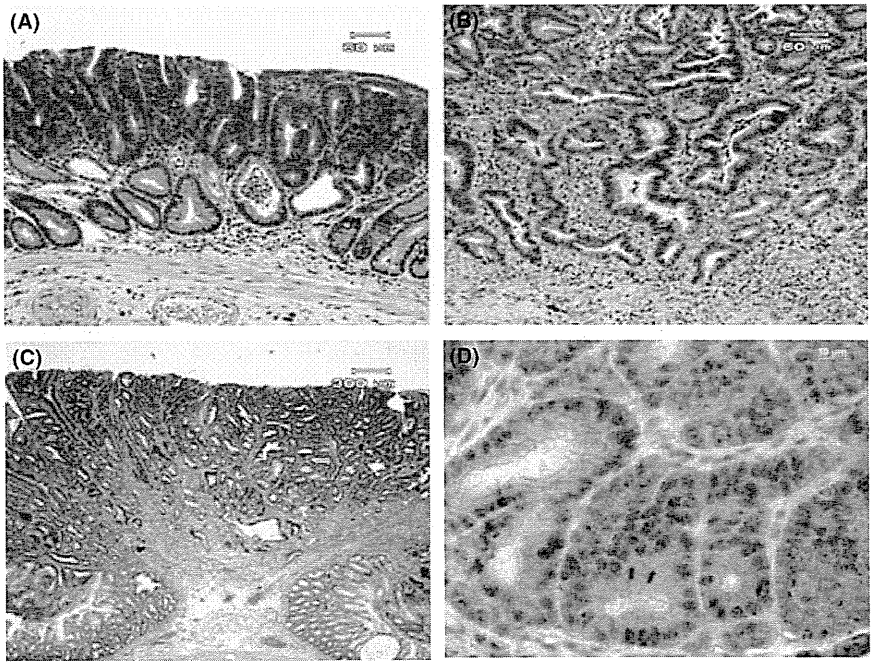

Fig. 5. Histopathology of colonic tumors developed in azoxymethane (AOM)/dextran sodium sulfate (DSS)-treated Kyoto Apc Delta (KAD) rats. (A) Tubular adenoma, (B) well-differentiated adenocarcinoma, and (C) moderately differentiated adenocarcinoma invading the submucosa. Hematoxylin–eosin stain. (D) β-Catenin immunohistochemistry in colonic adenocarcinoma.